Sintering temperature (°C)	Perovskite phase (%)	Tetragonality (c/a)	Relative density (%)	Grain size range (mean)* (μm)
1150	100	1.064	87	2.5–15.0 (6.5)
1175	100	1.064	89	8.0–26.5 (13)
1200	99.3	1.063	92	12.0–40.0 (29)
1225	90.1	1.063	94	20.0–65.0 (36)
1250	89.2	1.063	93	41.0–83.0 (52)

* The estimated precision of the grain size is ±10%

TABLE 1 Physical properties of singly sintered PT ceramics

T_1 (°C)	T_2 (°C)	Perovskite phase (%)	Tetragonality (c/a)	Relative density (%)	Grain size range (mean)* (μm)
700	1000	–	–	–	–
700	1050	–	–	–	–
700	1100	100	1.058	96	0.3–0.5 (0.3)
700	1150	100	1.060	96	0.3–1.2 (0.8)
700	1200	100	1.062	96	0.4–1.7 (1.3)
700	1250	–	–	–	–
800	1000	–	–	–	–
800	1050	100	1.064	95	1.0–2.2 (1.6)
800	1100	100	1.061	96	0.5–3.3 (1.9)
800	1150	100	1.060	96	1.0–2.7 (1.8)
800	1200	100	1.062	96	0.6–1.7 (1.2)
800	1250	–	–	–	–
900	1000	–	–	–	–
900	1050	100	1.060	96	0.4–2.2 (1.2)
900	1100	100	1.060	96	0.7–1.5 (1.1)
900	1150	100	1.057	96	0.6–1.9 (0.8)
900	1200	100	1.061	97	1.0–2.2 (1.5)
900	1250	100	–	–	–

* The estimated precision of the grain size is ±10%
– Data are not available because the samples were too fragile for the measurements

TABLE 2 Physical properties of doubly sintered PT ceramics

subjected to low sintering temperature, e.g. 1150 °C, eventually burst into pieces because of the internal anisotropic stress caused by the phase transition in the ceramics, as can be confirmed by the SEM images showing a loose formation of large grains (Fig. 4a and b), in agreement with high values of c/a given in Table 1. Additionally, average grain sizes were found to increase with the sintering temperature. For higher-temperature treatments, a pronounced second phase is segregated at the grain boundaries. The EDX spectra indicated that there was more Pb and less Ti in the bright region ([Pb] : [Ti] ∼ 4 : 1 at. %) than in the dark region ([Pb] : [Ti] ∼ 1 : 1 at. %), as shown in Fig. 4b–d. The observation of these (second-phase) layers could be attributed to a liquid-phase formation during the sintering process as proposed by many researchers [24, 25].

In addition, a combination of SEM and EDX techniques has demonstrated that small amounts of nanosized ($\varphi \sim 1.7$–2.5 nm) spherical TiO_2 inclusions (brighter phase) exist on the surface of perovskite PT grains in some samples, as shown in Fig. 4b and c, similar to those found by Takeuchi et al. [26]. The existence of a discrete TiO_2 phase points to the expected problem of poor homogeneity of the samples arising from PbO volatilization after being subjected to prolonged heating, although the concentration is too low for XRD detection.

Representative microstructures for doubly sintered PT ceramics are given in Fig. 5. The first sintering temperature was designed at 700, 800 and 900 °C, for constant dwell time and

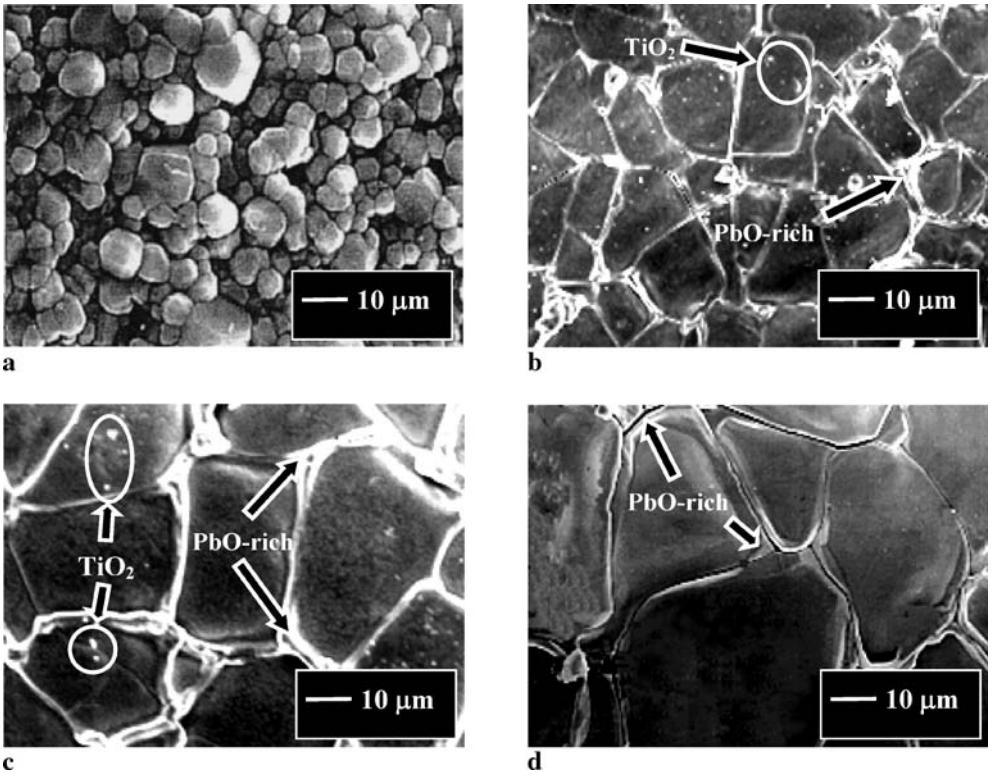

FIGURE 4 SEM micrographs of PT ceramics singly sintered at (**a**) 1150 (**b**) 1175 (**c**) 1200 and (**d**) 1225 °C

heating/cooling rates of 2 h and 1 °C/min at each stage, while the second sintering temperature was varied from 1100 °C to 1200 °C. It is seen that a uniform grain shape of typical perovskite ceramics [9, 22, 23] is observed, with sizes in the range of 0.4–2.0 μm. It should be noted that the average grain size of the doubly sintered PT ceramics is < 2.0 μm, which is less than the critical value of 3 μm reported by several workers [11, 26, 27]. Here, it is believed that smaller grains with random orientations result in lower internal stress in sintered samples because they compensate the anisotropy of thermal expansion coefficients.

By comparison with singly sintered PT ceramics, almost clean microstructures with high uniformity, denser angular grain packing and more homogeneity are generally observed in doubly sintered PT samples. These microstructures are typical of a solid-state sintering mechanism. In the present study (Fig. 5 and Table 2), the microstructural features of the doubly sintered PT ceramics with various second sintering temperatures ranging from 1050 to 1200 °C are not significantly different. However, it should be noted that higher angular grains were evidenced for higher second sintering temperature (see Fig. 5b, d and f). The observation that the sintering temperature effect may also play an important role in obtaining a high angularity in the grains of perovskite ceramics is also consistent with other similar systems [22, 23]. Moreover, an abnormal grain growth probably due to the inhibition of the normal grain growth mechanism during the double sintering process [14] was also found in some samples, as shown in Fig. 5c. It is also of interest to point out that evidence has been found for the existence of microcracks (arrowed) along the grain boundaries of the samples sintered at lower second sintering temperatures (Fig. 5c and e), in agreement with other works [9, 26, 28].

Interestingly, only the samples sintered at 700/1100–1200 °C, 800/1050–1200 °C or 900/1050–1200 °C with the highest relative density and smallest average grain size of about 95%–97% and 0.3–1.9 μm, respectively, remained unbroken. It may be simply assumed that the ceramics consisting of very fine grains have less elastic strain energy than the ceramics with significantly large grains (Tables 1 and 2). Consequently, the experimental work carried out here suggests that the optimum conditions for forming the highly dense PT ceramics in this work are double sintering temperatures at 700–900/1100–1200 °C, 2 h dwell time and 1 °C/min

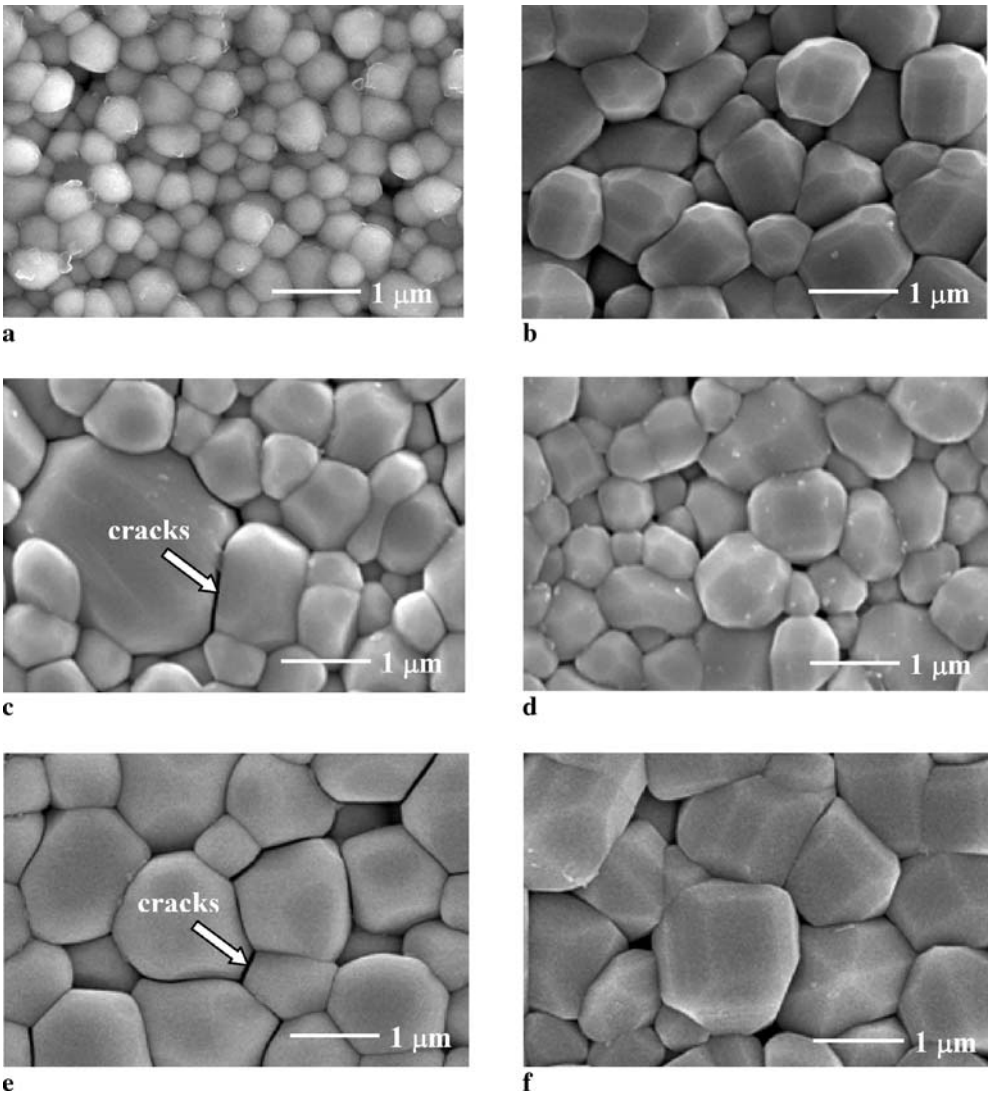

FIGURE 5 SEM micrographs of PT ceramics doubly sintered at (**a**) 700/1100 (**b**) 700/1200 (**c**) 800/1100 (**d**) 800/1200 (**e**) 900/1100 and (**f**) 900/1200 °C

heating/cooling rates. The different microstructure evolution of PT ceramics confirms the importance of the processing method. More importantly, considered from the perovskite content and microstructure of PT ceramics sintered by two different methods, the doubly sintered method was clearly preferable for obtaining dense perovskite PT ceramics. The following discussion of the dielectric properties of the PT ceramics obtained in this study would further support the advantage of the double sintering method.

The dielectric properties of the PT samples sintered with different techniques are also compared in Table 3, as well as in Fig. 6. The Curie temperatures are about the same for all samples measured, whilst the dielectric properties of both sets of the sintered PT ceramics seem to be different. As listed in Table 3, the room-temperature dielectric properties of the two sets of ceramics are not significantly different. The values of dielectric constant in the order of 200 are slightly higher than those reported earlier [9, 29]. However, the high-temperature dielectric properties of the doubly sintered PT samples are noticeably higher than those of the singly sintered PT samples, as seen in the inset of Fig. 6. As mentioned earlier, the reason for this is the high amount of secondary phase present in the singly sintered PT ceramics. In addition, a PbO-rich phase (as observed in Fig. 4b–d), with low dielectric constant, might be forming a continuous layer between grains and hence decreasing the dielectric constant of the singly sintered PT ceramics [13, 24, 30]. The secondary phases in singly sintered PT are interconnected at grain boundaries and, as suggested by Wang and Schulze [24], exert more influence on the dielectric properties than when they are isolated. It should also be noted that in singly sintered specimens the grain boundaries are mostly PbO-rich, while in doubly sintered specimens the grain boundaries are mainly PT with Pb/Ti ratio very close to 1. Although the number of grain boundaries increases in the doubly sintered ceramic, the improved properties are a result of a more chemical homogeneity of the microstructure in the doubly sintered ceramics. Therefore, in this study, it could be stated that the number of grain boundaries is not the main controlling factor for the properties in the doubly sintered ceramics, but the properties are rather dictated by the chemical composition of the grain boundaries.

Grain sizes also play a role in the difference in the dielectric properties, especially the dielectric constant. As clearly seen in Tables 1 and 2 (as well as Figs. 4 and 5), the larger grain size in the singly sintered ceramics would lead to lower dielectric constant than that of the doubly sintered ceramics. This relation is well established in several ceramic perovskite systems, e.g. $BaTiO_3$ [31], PZT ($Pb(Zr_{1/2}Ti_{1/2})O_3$) [32, 33], PMN [22, 34] and PFN [23].

The different microstructure and the different amount of secondary phases present in singly and doubly sintered PT ceramics strongly influence the dielectric properties of these materials, leading to superior electrical behaviour in doubly sintered PT ceramics. Moreover, this study demonstrated that the dielectric properties of PT ceramics are also influenced by microstructural features, especially the phase compositions at grain boundaries, microcracks and the densification mechanism rather than by only pyrochlore phase or by grain size itself.

Although a disadvantage of the proposed two-stage sintering method is a greater time requirement, the significant reduction in firing temperature is a positive development, par-

Dielectric Properties (1 MHz)	Sintering Condition (°C for 2 h) Single 1225	Single 700/1200	Double (T_1/T_2) 800/1200	Double (T_1/T_2) 900/1200
ε_r (25 °C)	243	209	255	209
tanδ(25 °C)	0.01	0.05	0.03	0.03
$\varepsilon_{r,max}$	7680	8993	8322	8198
tanδ_{max}	1.07	1.00	1.10	0.95
T_C	482	484	484	484

TABLE 3 Dielectric properties (at 1 MHz) of PT ceramics sintered at various conditions

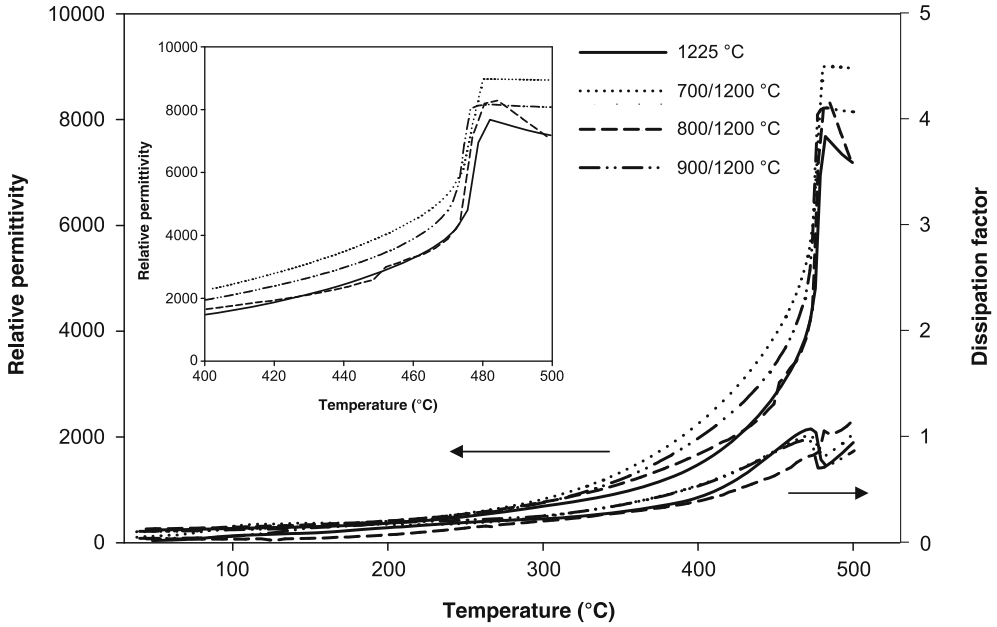

FIGURE 6 Variation with temperature of (**a**) relative permittivity (ε_r) and (**b**) dissipation factor (tanδ) at 1 MHz for PT ceramics sintered at various conditions (*inset*: relative permittivity vs temperature from 400 °C to 500 °C)

ticularly with regard to the drive towards electrodes of lower cost [1–3]. In general, these PT ceramics exhibit complex microstructures which are a result of variation in grain size and orientation, variation in chemical homogeneity, and the presence and distribution of additional minor phase, pores and (micro)cracks. These factors, which are strongly influenced by the sintering conditions, have an important effect on the dielectric properties of materials and their reproducibility.

4 Conclusion

The processing method used for preparing PT ceramics greatly influences the final properties of the ceramics. Even though the simple mixed oxide method employing conventional ball milling was used, this work demonstrated that it was possible to obtain rather dense PT ceramics with homogeneous microstructure by the two-stage sintering technique. It has been shown that, under suitable sintering conditions, the phase formation and densification of the ceramics are better than those obtained from the single-stage sintering. Reductions in the maximum required sintering temperature are possible as compared to the single-stage sintering.

ACKNOWLEDGEMENTS This work was supported by the National Nanotechnology Center (NANOTEC), the Faculty of Science and the Graduate School of Chiang Mai University.

REFERENCES

1 B. Jaffe, W.R. Cook, H. Jaffe, *Piezoelectric Ceramics* (Academic, New York, 1971)
2 G.H. Haertling, J. Am. Ceram. Soc. **82**, 797 (1999)
3 A.J. Moulson, J.M. Herbert, *Electroceramics*, 2nd edn. (Wiley, Chichester, 2003)
4 T. Takahashi, Am. Ceram. Soc. Bull. **69**, 691 (1990)
5 L.E. Cross, Mater. Chem. Phys. **43**, 108 (1996)
6 G. Shirane, S. Hoshino, J. Phys. Soc. Japan **6**, 265 (1951)
7 G. Shirane, R. Pepinsky, B.C. Frazer, Acta Crystallogr. **9**, 131 (1956)
8 H. Takeuchi, S. Jyomura, E. Yamamoto, Y. Ito, J. Acoust. Soc. Am. **72**, 1114 (1982)
9 L.B. Kong, W. Zhu, O.K. Tan, J. Mater. Sci. Lett. **19**, 1963 (2000)
10 T. Suwannasiri, A. Safari, J. Am. Ceram. Soc. **76**, 3155 (1993)
11 T. Takeuchi, M. Tabuchi, I. Kondoh, N. Tamari, H. Kageyama, J. Am. Ceram. Soc. **83**, 541 (2000)
12 J.S. Forrester, J.S. Zobec, D. Phelan, E.H. Kisi, J. Solid State Chem. **177**, 3553 (2004)
13 A. Udomporn, K. Pengpat, S. Ananta, J. Eur. Ceram. Soc. **24**, 185 (2004)
14 S. Ananta, N.W. Thomas, J. Eur. Ceram. Soc. **19**, 2917 (1999)
15 A. Udomporn, S. Ananta, Mater. Lett. **58**, 1154 (2004)
16 H. Klug, L.E. Alexander, *X-ray Diffraction Procedures for Polycrystalline and Amorphous Materials*, 2nd edn. (Wiley, New York, 1974)
17 R.L. Fullman, Trans. AIME **197**, 447 (1953)
18 JCPDS-ICDD card no. 6-452, International Centre for Diffraction Data, Newtown Square, PA, 2000
19 JCPDS-ICDD card no. 77-1971, International Centre for Diffraction Data, Newtown Square, PA, 2000
20 J. Tartaj, C. Moure, L. Lascano, P. Durán, Mater. Res. Bull. **36**, 2301 (2001)
21 M.L. Calzada, M. Alguero, L. Pardo, J. Sol-Gel Sci. Technol. **13**, 837 (1998)
22 S. Ananta, N.W. Thomas, J. Eur. Ceram. Soc. **19**, 629 (1999)
23 S. Ananta, N.W. Thomas, J. Eur. Ceram. Soc. **19**, 1873 (1999)
24 H.C. Wang, W.A. Schulze, J. Am. Ceram. Soc. **73**, 825 (1990)
25 S.M. Gupta, A.R. Kulkarni, J. Mater. Res. **10**, 953 (1995)
26 T. Takeuchi, M. Takahashi, K. Ado, N. Tamari, K. Ichikawa, S. Miyamoto, M. Kawahara, M. Tabuchi, H. Kageyama, J. Am. Ceram. Soc. **84**, 2521 (2001)
27 Y. Matsuo, H. Sasaki, J. Am. Ceram. Soc. **49**, 229 (1966)
28 S.R. Dhage, Y.B. Khollam, H.S. Potdar, S.B. Deshpande, B.D. Sarwade, D.K. Date, Mater. Lett. **56**, 564 (2002)
29 S. Chattopadhyay, P. Ayyub, V.R. Palkar, M. Multani, Phys. Rev. B **52**, 13177 (1995)
30 M. Villegas, A.C. Caballero, M. Kosec, C. Moure, P. Duran, J.F. Fernandez, J. Mater. Res. **14**, 891 (1999)
31 A. Yamaji, Y. Enomoto, K. Kinoshita, T. Murakami, J. Am. Ceram. Soc. **60**, 97 (1977)
32 B.M. Jin, J. Kim, S.C. Kim, Appl. Phys. A **65**, 53 (1997)
33 W. Cao, C.A. Randall, J. Phys. Chem. Solids **57**, 1499 (1996)
34 S.L. Swartz, T.R. Shrout, W.A. Schulze, L.E. Cross, J. Am. Ceram. Soc. **67**, 311 (1984)

Available online at www.sciencedirect.com
ScienceDirect
Materials Chemistry and Physics 102 (2007) 165–170
MATERIALS CHEMISTRY AND PHYSICS
www.elsevier.com/locate/matchemphys

Dielectric properties of $(1-x)Pb(Zr_{0.52}Ti_{0.48})O_3$–$(x)BaTiO_3$ ceramics under uniaxial compressive pre-stress

Rattikorn Yimnirun*, Supon Ananta, Sawarin Chamunglap

Department of Physics, Faculty of Science, Chiang Mai University, Chiang Mai 50200, Thailand

Received 30 May 2005; received in revised form 26 August 2006; accepted 29 November 2006

Abstract

Effects of uniaxial compressive pre-stress on the dielectric properties of ceramics in PZT–BT solid-solution system are investigated. The physical properties measurements reveal that the addition of BT into PZT results in the increase of grain size and microstructural heterogeneity, except for the density which sees the opposite trend. The dielectric properties measured under stress-free condition show a gradual increase of the dielectric constant with increasing BT content, while the dielectric loss tangent is not considerably different. The dielectric properties under the uniaxial compressive pre-stress of the PZT–BT ceramics are observed at stress levels up to 15 MPa using a uniaxial compressometer. The results clearly show that both the dielectric constant and the dielectric loss tangent of the PZT–BT ceramics increase significantly with increasing applied stress. Larger changes in the dielectric properties with the applied stress are observed in the PZT-rich compositions. The experimental observations have been attributed to the increase of the domain wall motions from the application of the compressive pre-stress.

Keywords: Uniaxial stress; Dielectric properties; PZT–BT

1. Introduction

Along with nanotechnology, smart materials and systems have recently been identified as the next generation technology [1–3]. Among many smart systems, piezoelectric ceramic actuators and transducers are finding an increasingly wide range of applications. In most applications, ceramics are often subjected to mechanical loading, either deliberately in the design of the device itself or because the device is used to change shapes as in many smart structure applications or the device is used under environmental stresses. In some cases, due to the piezoelectric nature of a material used within, the devices are also subjected to the self-induced internal stress [2–4]. A prior knowledge of how the materials behave under different load conditions is therefore very crucial for proper design of a device and for suitable selection of materials for a specific application. Therefore, it is very important to determine the properties of these materials as a function of applied stress. Previous investigations on the stress-dependence dielectric and electrical properties of many ceramic systems, such as PZT, PMN–PZT and PMN–PT have clearly emphasized the importance of the subject [4–11].

Among perovskite ferroelectric materials, lead zirconate titanate ($Pb(Zr_{1-x}Ti_x)O_3$ or PZT) and barium titanate ($BaTiO_3$ or BT) ceramics have been investigated extensively and continuously since the late 1940s [12–15]. PZT and BT are representative perovskite piezoelectric and ferroelectric prototypes, respectively, because of their excellent electrical properties. These two ceramics possess distinct characteristics that make each ceramic suitable for different applications. One of the most studied piezoelectric compounds, $Pb(Zr_{0.52}Ti_{0.48})O_3$, a morphotropic phase boundary (MPB) compound of PZT, has great piezoelectric properties with a high Curie temperature (T_C) of ~390 °C. BT exhibits high dielectric constant and superior electrostrictive responses with a lower T_C (~120 °C) [12–15]. In addition, BT is mechanically superior than PZT [16], whereas PZT ceramics can be easily sintered at temperature much lower than BT ceramics, which usually require as high sintering temperature as 1400 °C [16]. With their complementary features, the solid solutions between PZT and BT are expected to exhibit better properties than those of the single-phase PZT and BT [12–15]. Furthermore, the properties can also be tailored over a wider range by changing the compositions to meet the strict

* Corresponding author. Tel.: +66 53943367; fax: +66 53943445.
E-mail address: rattikornyimnirun@yahoo.com (R. Yimnirun).

0254-0584/$ – see front matter © 2006 Elsevier B.V. All rights reserved.
doi:10.1016/j.matchemphys.2006.11.021

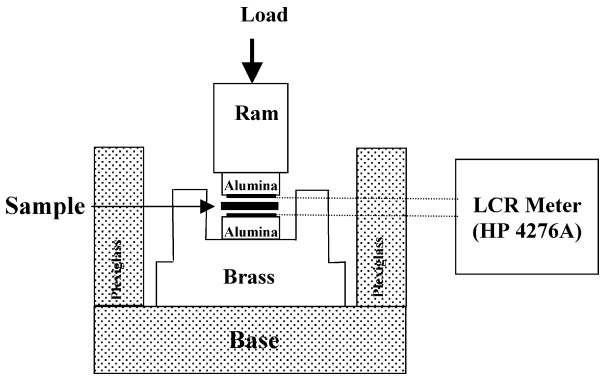

Fig. 1. A schematic of the experimental set-up.

requirements for specific applications [3,12–15]. Prior investigations have already revealed interesting results on the structure, and the dielectric and ferroelectric properties of the PZT–BT solid solutions [16–18]. However, there has been no report on the influences of the applied stress on the electrical properties of the PZT–BT systems. Therefore, this study is undertaken to investigate the influences of the uniaxial compressive pre-stress on the dielectric properties of $(1-x)$PZT–xBT ceramic systems.

2. Experimental

The $(1-x)Pb(Zr_{0.52}Ti_{0.48})O_3$–$(x)BaTiO_3$ ceramic systems used in this study are prepared from the PZT and BT starting powders by a mixed-oxide method. The precursor PZT and BT powders are first prepared from reagent-grade PbO (99%), ZrO_2 (99%) and TiO_2 (99%), and $BaCO_3$ (99%) and TiO_2 (99%) starting powders, respectively. These powders are ball-milled for 24 h and later calcined for 2 h at 900 °C for PZT and at 1300 °C for BT. Subsequently, the $(1-x)Pb(Zr_{0.52}Ti_{0.48})O_3$–$(x)BaTiO_3$ (when $x = 0.0, 0.05, 0.15, 0.25, 0.35, 0.45, 0.55, 0.65, 0.75, 0.85, 0.95$ and 1.0) ceramics are prepared from the starting PZT and BT powders by a mixed-oxide method at various processing conditions. Initially, the PZT and BT powders for a given composition are weighed and then ball-milled in ethanol for 24 h. After drying process, the mixed powders are pressed hydraulically to form disc-shaped pellets 10 mm in diameter and 2 mm thick, with 5 wt.% polyvinyl alcohol (PVA) as a binder. The pellets are stacked in a covered alumina crucible filled with PZ powders to prevent lead loss. Finally, the sintering is carried out at a sintering temperature for 2 h with 5 min °C^{-1} heating and cooling rates. The firing profile includes a 1-h dwell time at 500 °C for binder burnout process to complete. For optimization purpose, the sintering temperature is varied between 1050 and 1400 °C depending upon the compositions. The densities of the sintered ceramics are measured by Archimedes method. The phase formations of the sintered specimens are studied by an X-ray diffractometer (Philips Analytical). The microstructure analyses are undertaken by a scanning electron microscopy (SEM: JEOL Model JSM 840A). Grain size is determined from SEM micrographs by a linear intercept method. The detailed descriptions of powders and ceramics processing and characterizations are presented thoroughly in the earlier publication [16].

For dielectric property characterizations under a uniaxial compressive pre-stress, the sintered samples are lapped to obtain parallel faces disc-shaped specimens with diameter of 10 mm and thickness of 2 mm, and the faces are then coated with silver paint as electrodes. The samples are then heat-treated at 750 °C for 12 min to ensure the contact between the electrodes and the ceramic surfaces. The samples are subsequently poled in a silicone oil bath at a temperature of 120 °C by applying a dc field of 20 kV cm^{-1} for 30 min. To study the effects of the uniaxial compressive pre-stress on the dielectric properties, the uniaxial compressometer is constructed [10,11]. As shown in Fig. 1, the compressometer is developed for simultaneous applications of the mechanical stress and the electric field. The compressometer cell consisting of a cylindrical brass cell with a heavy brass base, a brass ram and a precisely guided loading platform provides true uniaxial stress during mechanical loading. The prepared specimen is carefully placed between the two alumina blocks and the electric field is applied to the specimen via the copper shims attached to the alumina blocks. With this setting, the uniaxial compressive stress is applied parallel to the electric field direction. The uniaxial compressive stress is supplied by the servohydraulic load frame and the applied stress level is monitored with the pressure gage of the load frame. Measurements are performed as a function of mechanical pre-stress applied discretely between 0 and 15 MPa. The measurements are carried out on the samples for loading and unloading conditions. Each measurement is repeated two to three times to ensure the reliability of the experimental results. During the measurements, a desired pre-stress is first applied to the sample and the dielectric properties are then recorded. The dielectric properties are measured through the LCZ-meter (Hewlett Packard, model 4276A). The capacitance and the dielectric loss tangent are determined at frequency of 1 kHz and room temperature (25 °C). The dielectric constant is then calculated from a parallel-plate capacitor equation, e.g. $\varepsilon_r = Cd/\varepsilon_0 A$, where C is the capacitance of the sample, d and A the thickness and the area of the electrode, respectively, and ε_0 is the dielectric permittivity of vacuum (8.854×10^{-12} F m^{-1}).

3. Experimental results

The phase formation behavior of the sintered ceramics is revealed by an XRD method. The XRD patterns, shown in Fig. 2, show that the sintered ceramics are clearly in perovskite phase. From the XRD patterns, PZT and BT ceramics are both identified as a single-phase material with a perovskite structure having tetragonal symmetry [16]. The patterns can be matched with JCPDF files no 33-0784 and 79-2264 for PZT and BT, respectively. For other PZT–BT compositions, the diffraction peaks move gradually towards higher angles with increasing BT contents, indication of smaller cell parameters. It should also be noticed that compositions with $0.45 \leq x \leq 0.75$ exhibit evidence of a possible rhombohedral structure with no clear splitting of peaks around 2θ of 43–46°. However, it is still clearly seen from the XRD patterns that PZT–BT forms a series of continuous solid solutions [16].

The optimized density of sintered $(1-x)$PZT–xBT ceramics is listed in Table 1. It is observed that an addition of BT to the PZT–BT compositions results in a continual decrease in the density of the ceramics from, in the units of gram per centimeter

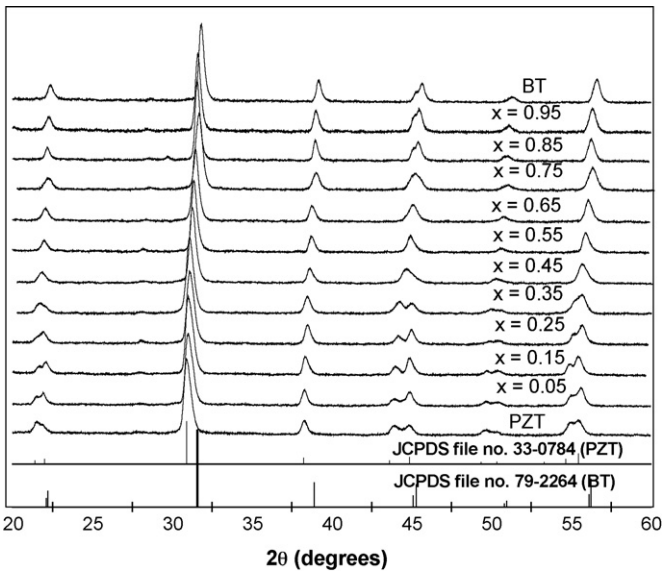

Fig. 2. XRD diffraction patterns of the sintered $(1-x)$PZT–(x)BT ceramics.

Table 1
Microstructural and dielectric features of $(1-x)$PZT–xBT ceramics

Ceramic	Density (g cm^{-3})	Grain size range (μm)	Average grain size (μm)	Stress-free ε_r (25 °C/1 kHz)	Stress-free tan δ (25 °C/1 kHz)
PZT	7.75	1–5	1.89 ± 0.52	813	0.011
0.95PZT–0.05BT	7.67	1–4	1.66 ± 0.32	809	0.007
0.85PZT–0.15BT	7.42	1–5	2.40 ± 0.58	839	0.006
0.75PZT–0.25BT	7.30	1–3	1.91 ± 0.47	857	0.004
0.65PZT–0.35BT	6.99	1–4	2.36 ± 0.71	875	0.005
0.55PZT–0.45BT	6.78	1–6	2.93 ± 0.53	890	0.006
0.45PZT–0.55BT	6.63	1–7	3.17 ± 0.72	952	0.005
0.35PZT–0.65BT	6.38	1–10	4.42 ± 0.79	1060	0.007
0.25PZT–0.75BT	6.28	1–10	3.28 ± 0.53	1077	0.005
0.15PZT–0.85BT	6.07	1.5–9	3.52 ± 0.77	1223	0.004
0.05PZT–0.95BT	5.95	2–10	4.86 ± 0.88	1288	0.005
BT	5.35	7–12	10.82 ± 0.53	1429	0.004

cube, 7.75 for PZT to 5.35 for BT. This is clearly due to the fact that BT has lower density than PZT. Except for BT which has a density of 89% of the theoretical density, all other ceramics are well sintered with high density (as high as 96% of the theoretical density in PZT ceramic). Relatively low density observed in BT ceramic is a result of porous and non-uniform microstructure, as seen from SEM micrograph in Fig. 3(f). For BT-rich compositions, SEM micrographs also show porous microstructure which

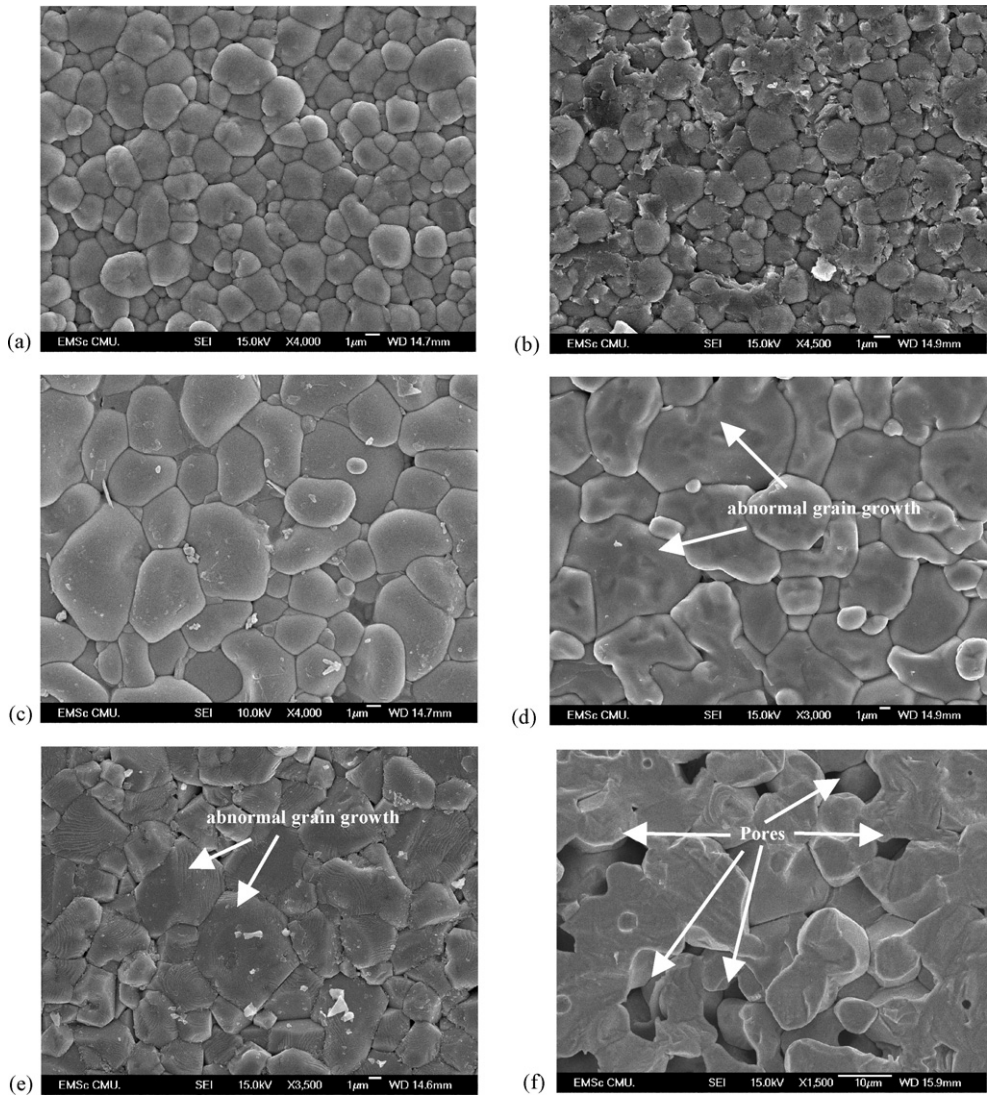

Fig. 3. SEM micrographs of $(1-x)$PZT–xBT ceramics: (a) PZT; (b) 0.75PZT–0.25BT; (c) 0.55PZT–0.45BT; (d) 0.35PZT–0.65BT; (e) 0.15PZT–0.85BT; (f) BT.

could be attributed to PbO loss during high sintering temperatures required for these compositions. In addition, an abnormal grain growth observed in the BT-rich compositions is probably due to the fact that the sintering temperatures required for highest densification for PZT and BT ceramics are very different, which could lead to distinctive grain growth behaviors between two phases [16]. Hence, the heterogeneous microstructure with a large grain size range is observed for BT-rich ceramic compositions, as seen in Fig. 3(d and e) and as listed in Table 1. On the other hand, PZT-rich compositions exhibit more uniform microstructure with the average grain size in the range of 1–3 μm. Moreover, the average grain size of the whole compositional range increases significantly from <2 μm in PZT to >10 μm in BT, as tabulated in Table 1.

The room temperature dielectric properties measured under stress-free condition are also listed in Table 1. It is clearly seen that dielectric constant (ε_r) of $(1-x)$PZT–xBT ceramics increases with increasing BT content. The dielectric constant increases from 813 in PZT to 1429 in BT. The increase of the dielectric constant within the compositional range is due to the high dielectric constant of BT [12–15]. When compared to PZT, higher dielectric constant observed in BT at room temperature is a result of its two ferroelectric transition temperatures at 0 and 120 °C [13–15]. However, the stress-free dielectric loss tangent ($\tan\delta$) does not change significantly with compositions. The relatively higher value of dielectric loss tangent of 0.011 for PZT is probably due to more domain wall motions expected in piezoelectric PZT as compared to piezoelectrically less active BT [6,19,20]. Similar dielectric behaviors have been reported in other solid-solution systems, such as PZN–BT [21], PMN–PZT [22] and PNN–PZT [23].

The experimental results of the uniaxial compressive pre-stress dependence of the dielectric properties of the ceramics in PZT–BT system are shown in Figs. 4 and 5. There is a significant change of both the dielectric constant and the dielectric loss tangent of the ceramics when the applied stress increases from 0 to 15 MPa. The changes of the dielectric constant with the applied stress can be divided into three different groups.

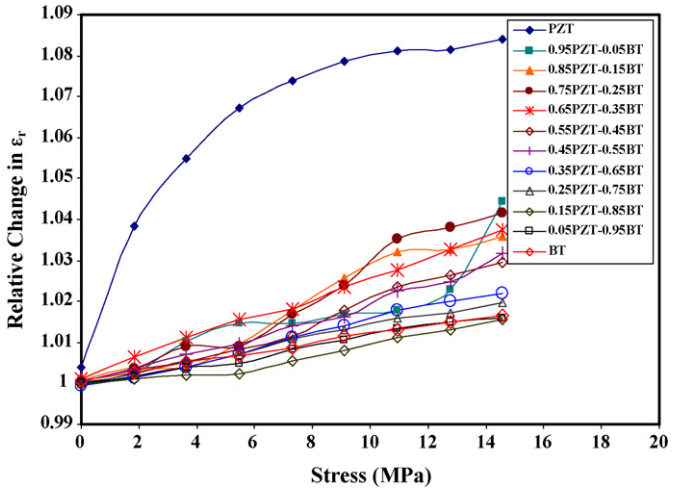

Fig. 4. Relative changes of dielectric constant (ε_r) as a function of compressive pre-stress for $(1-x)$PZT–(x)BT ceramics.

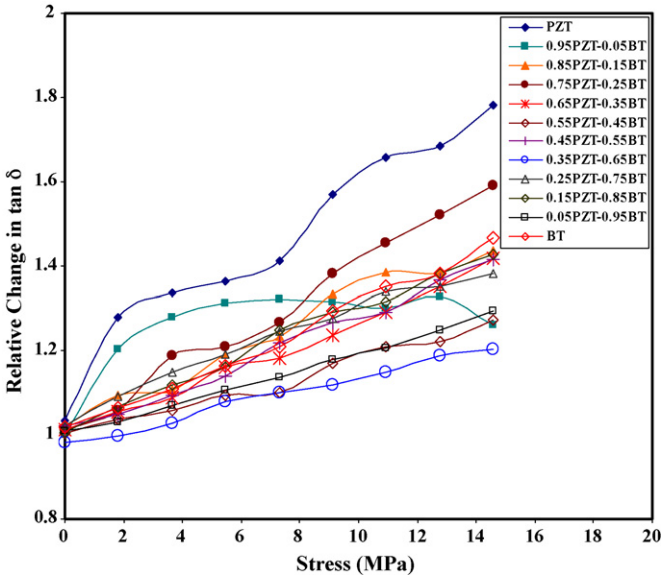

Fig. 5. Relative changes of dielectric loss tangent ($\tan\delta$) as a function of compressive pre-stress for $(1-x)$PZT–(x)BT ceramics.

For PZT ceramic, the dielectric constant increases exponentially with applied stress. It can be seen that dielectric constant is enhanced by approximately 8% at 15 MPa applied stress. For PZT-rich compositions (0.95PZT–0.05BT, 0.85PZT–0.15BT, 0.75PZT–0.25BT, 0.65PZT–0.35BT and 0.55PZT–0.45BT), the dielectric constant increases rather linearly with increasing applied stress. The changes in the dielectric constant between 2 and 4% at 15 MPa applied stress are obviously smaller than that observed in PZT. For BT-rich compositions (BT, 0.05PZT–0.95BT, 0.15PZT–0.85BT, 0.25PZT–0.75BT and 0.35PZT–0.65BT), the dielectric constant only rises slightly (<2%) and in a linear manner when the applied stress increases to the maximum amplitude. The dielectric loss tangent for all compositions is found to increase significantly and non-linearly when the applied stress is raised from 0 to 15 MPa. The largest changes occur in PZT and 0.75PZT–0.25BT with the dielectric loss tangent enhancement of nearly 80 and 50%, respectively. For other compositions, the increase in the dielectric loss tangent varies between 10 and 40% at 15 MPa applied stress. Again the changes of the dielectric loss tangent of BT-rich compositions are comparatively smaller than those of PZT-rich compositions, similar to what have been observed in the case of the dielectric constant. Similar experimental results have been reported previously for soft PZT [9,24], un-doped PZT with various Zr/Ti ratio [25], and Ca-doped BT [26], in which the dielectric properties are found to increase with increasing magnitude of the compressive pre-stress.

To understand these experimental results, various effects have to be considered. Normally, the properties of ferroelectric materials are derived from both the intrinsic contribution, which is the response from a single domain, and extrinsic contributions, which are from domain wall motions [19,25–27]. When a mechanical stress is applied to a ferroelectric material, the domain structure in the material will change to maintain the domain energy at a minimum; during this process, some of

the domains engulf other domains or change shape irreversibly. Under a uniaxial stress, the domain structure of ferroelectric ceramics may undergo domain switching, clamping of domain walls, de-aging and de-poling [20,27]. In this study, the results on the uniaxial compressive pre-stress dependence of the dielectric properties can easily be explained with the above statements. When the compressive uniaxial stress is applied in the direction parallel to the polar axis (poling) direction, the stress will move some of the polarization away from the poling direction resulting in a change in domain structures [6,25–27]. This change increases the non-180° domain wall density. Hence, the increase of the dielectric constant with the applied stress is observed. The de-aging mechanism is also expected to play a role here. However, the stress clamping of domain walls and the de-poling mechanisms are not expected at this relatively low stress level used in this study [6,27]. Therefore, a combination of the domain switching and the de-aging mechanisms is believed to be a reason for the increase of the dielectric constant with increasing applied stress in the PZT–BT system, as shown in Fig. 4. The cause of the stress dependence of the dielectric loss tangent is a little more straightforward than that of the dielectric constant. Stress-induced de-pinning of the domain walls is expected to occur under the applied compressive pre-stress. As depicted in Fig. 5, an increase in domain wall mobility clearly enhances the dielectric loss tangent in all compositions [19,20,27]. Additionally, it should also be noticed that pure PZT obtained from this study has a tetragonal structure and is supposed to be hard to switch its polarization. In comparison, as described earlier the compositions $x = 0.45$ and 0.75 seem to be MPB compositions between tetragonal and rhombohedral PZT phases, thus high response to external stress is expected in these two compositions. However, the experimental results did not show the high dielectric response to stress, as seen in Figs. 4 and 5. This interesting observation could be explained as follows. Since the two compositions are seen to exhibit the co-existence of both tetragonal and rhombohedral PZT phases, one would expect to observe enhanced properties, as observed in PZT [3,15]. However, the dielectric properties observed in this PZT–BT system are not seen to enhance at the two MPB compositions, as listed in Table 1. This is probably because the dielectric properties are not entirely controlled by the chemical composition, but also dictated by other factors, such as microstructure and chemical homogeneity [14,15]. Since BT requires significantly higher sintering temperature than does PZT, very different microstructures are observed in pure PZT and PZT–BT compositions, as evident from grain size variation listed Table 1, and abnormal grain-growth behavior and porous microstructure displayed in Fig. 3. These features clearly suppress the dielectric properties of the MPB compositions [28,29]. This observation also suggests that the dielectric responses to the external stress are not controlled exclusively by the intrinsic contribution from single domain, but the main contribution may arise from the extrinsic contributions from domain wall motions, which could be heavily clamped by inhomogeneous microstructures [19,27]. Therefore, this explains relatively low dielectric responses to the stress in the two MPB compositions. Similar observations have been reported in the MPB compositions in PZT–PMN [30,31] and PMN–PT [32]. Finally, it should be noted here that the dielectric behaviors under the applied stress for PZT–BT system are significantly different from those observed in a solid solution between normal and relaxor ferroelectrics, i.e. PZT–PMN systems, in which the dielectric responses to the applied stress depend more on the compositions and the stress level, and the dielectric properties of some compositions decrease with increasing applied stress [10].

4. Conclusions

In this study, effects of uniaxial compressive pre-stress on the dielectric properties of ceramics in PZT–BT system are investigated. The $(1-x)Pb(Zr_{0.52}Ti_{0.48})O_3$–$(x)BaTiO_3$ (when $x = 0.0$, 0.05, 0.15, 0.25, 0.35, 0.45, 0.55, 0.65, 0.75, 0.85, 0.95 and 1.0) ceramics used are prepared by a conventional mixed-oxide method from starting PZT and BT powders at various processing conditions. The phase formation behavior studied using the XRD indicates that PZT–BT forms a series of continuous solid solutions. The physical properties measurements reveal that the properties are relatively composition-dependent. Except for the density which sees the opposite trend, the addition of BT into PZT results in the increase of grain size and microstructural heterogeneity. The dielectric properties measured under stress-free conditions show a gradual increase of the dielectric constant with increasing BT content, while the dielectric loss tangent is not significantly different. The dielectric properties under the uniaxial compressive pre-stress of the PZT–BT ceramics are observed at stress levels up to 15 MPa using a uniaxial compressometer. The results clearly show that both the dielectric constant and the dielectric loss tangent of the PZT–BT ceramics increase significantly with increasing applied stress. Larger changes in the dielectric properties with the applied stress are observed in the PZT-rich compositions. The experimental observations have been attributed to the increase of the domain wall motions from the application of the compressive pre-stress.

Acknowledgment

Financial support from the Thailand Research Fund (TRF) is gratefully acknowledged.

References

[1] N. Setter, R. Waser, Acta Mater. 48 (2000) 151.
[2] N. Setter, J. Eur. Ceram. Soc. 21 (2001) 1279.
[3] L.E. Cross, Ferroelectrics 76 (1987) 241.
[4] D. Viehland, J. Powers, J. Appl. Phys. 89 (2001) 1820.
[5] J. Zhao, A.E. Glazounov, Q.M. Zhang, Appl. Phys. Lett. 74 (1999) 436.
[6] Q.M. Zhang, J. Zhao, K. Uchino, J. Zheng, J. Mater. Res. 12 (1997) 226.
[7] D. Viehland, J. Powers, Appl. Phys. Lett. 78 (2001) 3112.
[8] D. Viehland, J.F. Li, E. McLaughlin, J. Powers, R. Janus, H. Robinson, J. Appl. Phys. 95 (2004) 1969.
[9] D. Zhou, M. Kamlah, D. Munz, J. Eur. Ceram. Soc. 25 (2005) 425.
[10] R. Yimnirun, S. Ananta, E. Meechoowas, S. Wongsaenmai, J. Phys. D: Appl. Phys. 36 (2003) 1615.
[11] R. Yimnirun, S. Ananta, A. Ngnamjarurojana, S. Wongsaenmai, Appl. Phys. A 81 (2005) 1227.
[12] G.H. Haertling, J. Am. Ceram. Soc. 82 (1999) 797.

[13] L.E. Cross, Mater. Chem. Phys. 43 (1996) 108.
[14] A.J. Moulson, J.M. Herbert, Electroceramics: Materials, Properties, Applications, second ed., John Wiley & Sons Ltd., 2003.
[15] B. Jaffe, W.R. Cook, Piezoelectric Ceramics, R.A.N. Publishers, 1971.
[16] W. Chaisan, R. Yimnirun, S. Ananta, D.P. Cann, Mater. Lett. 59 (2005) 3732.
[17] B.K. Gan, J.M. Xue, D.M. Wan, J. Wang, Appl. Phys. A 69 (1999) 433.
[18] F. Xia, X. Yao, J. Mater. Sci. 34 (1999) 3341.
[19] G. Yang, W. Ren, S.F. Liu, A.J. Masys, B.K. Mukherjee, Proc. IEEE Ultrason. Symp. (2000) 1005.
[20] O. Steiner, A.K. Tagantsev, E.L. Colla, N. Setter, J. Eur. Ceram. Soc. 19 (1999) 1243.
[21] A. Halliya, U. Kumar, R.E. Newnham, L.E. Cross, Am. Ceram. Soc. Bull. 68 (1987) 671.
[22] R. Yimnirun, S. Ananta, P. Laoratanakul, J. Eur. Ceram. Soc. 25 (2005) 3225.
[23] N. Vittayakorn, G. Rujijanagul, X. Tan, M.A. Marquadrt, D.P. Cann, J. Appl. Phys. 96 (2004) 5103.
[24] J.M. Calderon-Moreno, Mater. Sci. Eng. A 315 (2004) 227.
[25] D. Audigier, Cl. Richard, Cl. Descamps, M. Troccaz, L. Eyraud, Ferroelectrics 154 (1994) 219.
[26] I.J. Fritz, J. Appl. Phys. 49 (1978) 4922.
[27] G. Yang, S.F. Liu, W. Ren, B.K. Mukherjee, Proc. SPIE Symp. Smart Struct. Mater. 3992 (2000) 103.
[28] W. Chaisan, R. Yimnirun, S. Ananta, D.P. Cann, Mater. Sci. Eng. B 132 (2006) 300.
[29] S. Wongsaenmai, Y. Laosiritaworn, S. Ananta, R. Yimnirun, Mater. Sci. Eng. B 128 (2006) 83.
[30] R. Yimnirun, S. Ananta, A. Ngamjarurojana, S. Wongsaenmai, Curr. Appl. Phys. 6 (2006) 520.
[31] R. Yimnirun, Ferroelectrics 331 (2006) 9.
[32] R. Yimnirun, M. Unruan, Y. Laosiritaworn, S. Ananta, J. Phys D: Appl. Phys. 39 (2006) 3097.

Temperature scaling of dynamic hysteresis in soft lead zirconate titanate bulk ceramic

R. Yimnirun,[a] R. Wongmaneerung, S. Wongsaenmai, A. Ngamjarurojana, S. Ananta, and Y. Laosiritaworn
Department of Physics, Faculty of Science, Chiang Mai University, Chiang Mai 50200, Thailand

(Received 15 November 2006; accepted 8 February 2007; published online 13 March 2007)

The temperature scaling of the dynamic hysteresis was investigated in soft ferroelectric bulk ceramic. The power-law temperature scaling relations were obtained for hystersis area $\langle A\rangle$ and remnant polarization P_r, while the coercivity E_C was found to scale linearly with temperature T. The three temperature scaling relations were also field dependent. At fixed field amplitude E_0, the scaling relations take the forms of $\langle A\rangle \propto T^{-1.1024}$, $P_r \propto T^{-1.2322}$, and $(E_{C0}-E_C)\propto T$. Furthermore, the product of P_r and E_C also provides the same scaling law on the T dependence in comparison with $\langle A\rangle$.
 [DOI: 10.1063/1.2713336]

Soft lead zirconate titanate [$Pb(Zr_{1-x}Ti_x)O_3$ or PZT] ceramics have been employed extensively in sensors and actuators. In these applications, the dynamic hysteresis characteristics have become an important consideration.[1] Theoretical studies have been carried out to understand the dynamic response of hysteresis curves in spin and polarization systems.[2–5] In particular, attention is focused on scaling law $\langle A\rangle \propto f^m E_0^n$ (where $\langle A\rangle$ is hysteresis area, E_0 is field amplitude, f is frequency, and m and n are exponents that depend on the dimensionality and symmetry of the system). Experimental investigations on a few thin-film systems have also been reported.[6–12] Recently, the scaling relation for soft PZT bulk ceramic was reported in the form of $\langle A\rangle \propto f^{-0.25}E_0$.[13] We also reported the stress-dependent scaling relation in the form of $\langle A-A_{\sigma=0}\rangle \propto f^{-0.25}E_0\sigma^{0.44}$, which indicates the difference of the energy dissipation between the under stress and stress-free conditions.[14] More importantly, it is well known that the size and shape of the hysteresis loop in the ferroelectric state depend strongly on temperature T.[1,15] The temperature dependence of ferroelectric properties is of interest in view not only of technological applications, but also in a fundamental sense.[16–22] The theoretical investigation by Rao *et al.*[2] has already proposed a temperature scaling for ferromagnetic materials, which indicates that the hysteresis area decreases with increasing temperature. Experimental results on ferromagnetic thin films have revealed various temperature scaling relations.[2,3,6,8] Interestingly, there has been no report on the temperature scaling of dynamic hysteresis in ferroelectrics, both theoretically and experimentally. It is therefore the aim of this study to experimentally establish the temperature scaling of the ferroelectric hysteresis for soft PZT bulk ceramic.

The polarization–electric field (P-E) hysteresis loops of commercial soft PZT ceramic disks (APC-855, APC International, Ltd., USA) with diameter of 8 mm and thickness of 1 mm were obtained by a standardized ferroelectric testing unit, RT66A (Radiant Technologies Inc., NM), over the temperature range 298–453 K with E_0 up to 40 kV/cm (f was fixed at 4 Hz). The measurements were performed on three ceramic disks. The Curie temperature (T_C) of the soft PZT used was experimentally determined from dielectric measurement to be 523 K. Other basic properties provided by the supplier are dielectric constant (1 kHz) $\varepsilon_r=3400$, piezoelectric strain constants $d_{33}=600$ pm/V and $d_{31}=-276$ pm/V, planar coupling factor $k_p=0.68$, and mechanical quality factor $Q_m=65$. It should also be noted that after being subjected to the hysteresis measurements, the samples showed a reduction of 10% in ε_r value and of 30% in d_{33} value.

Figure 1 displays the hysteresis loop profile for various electric field amplitudes E_0 at a fixed $T=373$ K [Fig. 1(a)] and for various temperatures at a fixed $E_0=40$ kV/cm [Fig. 1(b)]. From the P-E loops, it is obvious that both E_0 and T play a crucial role on the hysteresis area $\langle A\rangle$. Similar observations have been reported in many other ferroelectric systems.[12,18,20,22] More interestingly, the observed temperature dependence of these hysteresis parameters prompts a question of whether there exist temperature scaling relations for these parameters.

Figure 2 shows the relation between $\langle A\rangle$ and T in a double logarithmic form, where good linear fits are apparent (R^2 close to 1). This implies a power-law relation between the hysteresis area and temperature, i.e., $\langle A\rangle \propto T^{\gamma}$, and for each E_0, the exponent γ can be extracted from the slope, i.e., $\gamma = d\ln\langle A\rangle / d\ln T$. However, both the slope γ and the y intercept seem to vary with E_0. Thus, to prove this E_0 dependence, both the slope γ and the y intercept are plotted as a function of E_0 (insets in Fig. 2), and the linear dependences on E_0 are noticeable. The linear least square fits of both slopes and y intercepts with E_0 give $y=-0.0332x-1.1024$ with $R^2=0.9983$ for the slope (lower inset) and $y=0.0769x+6.0137$ with $R^2=0.9966$ for the y intercept (upper inset). However, the y intercept refers to the value of $\ln\langle A\rangle$ at the limit $\ln T$ approaching zero, and from the fitting, $\ln\langle A\rangle$ is not ceased at this limit, which is not really sound because at low temperatures the dynamics of the dipoles or domain walls is frozen. This could be due to the fact that the domain wall motion at high temperature is very different from those at very low temperature.[23,24] Consequently, this study does not imply if there is a finite hysteresis area at T approaching zero (i.e., in this case $\ln T=0$ or $T=1$), but the quantity $\ln\langle A\rangle$ at $\ln T=0$ here comes from an empirical fit to fulfill the validity of the linear fit. Therefore, based on the proposed assump-

[a]Author to whom correspondence should be addressed; electronic mail: rattikornyimnirun@yahoo.com

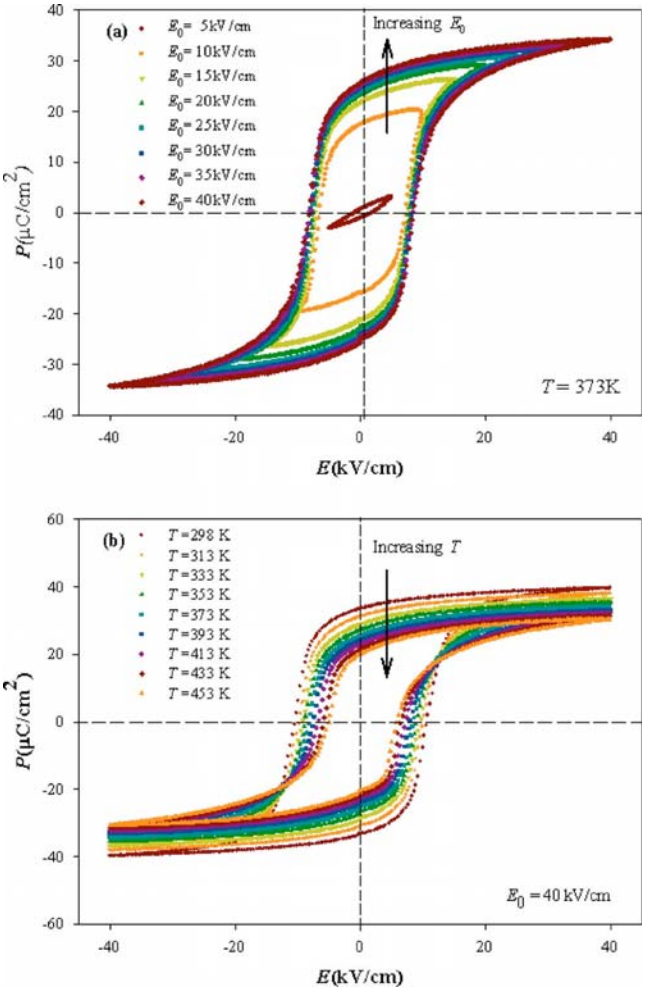

FIG. 1. Hysteresis loops for soft PZT ceramic (a) at T=373 K with varying E_0, and (b) at E_0=40 kV/cm with varying T.

tions and fitting techniques, and by integrating all the relevant fits, it is found that

$$\langle A\rangle = \exp(0.0769E_0 + 6.0137)T^{-(0.0332E_0+1.1024)}. \quad (1)$$

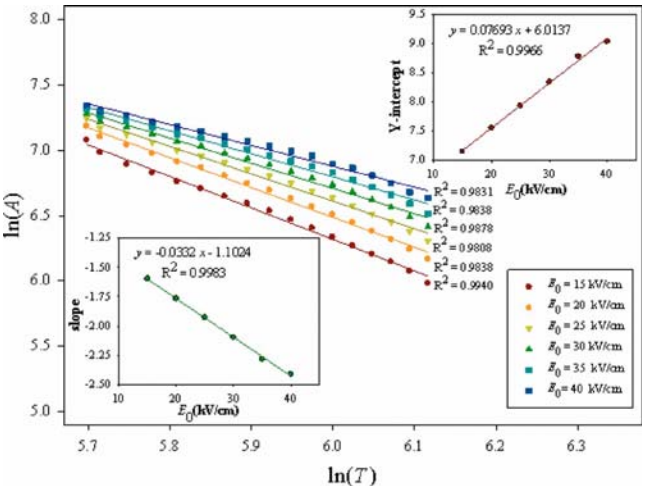

FIG. 2. Double logarithmic plot between ln(A) and ln(T) for various E_0, where the linear relations are found but the y intercepts and slopes seem to be E_0 dependent. The insets show those linear relations with E_0.

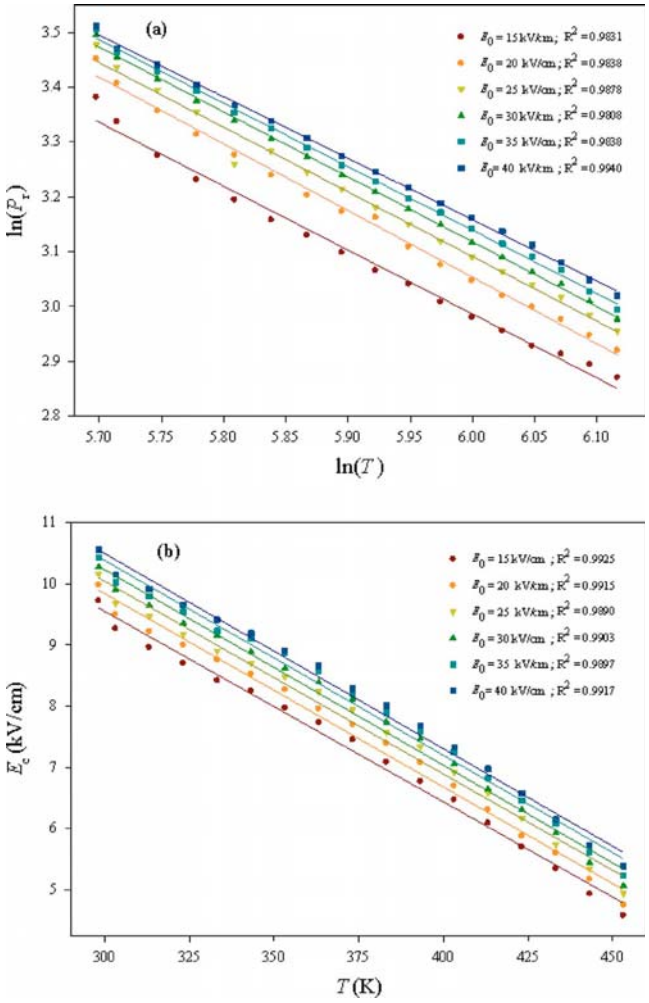

FIG. 3. (a) Double logarithmic plot between ln(P_r) and ln(T), and (b) linear plot between E_C and T.

Through similar mathematical treatment performed on $\langle A\rangle$, temperature-dependent relations for remnant polarization (P_r) and coercivity (E_C) are also obtained. Figure 3(a) shows the relation between P_r and T in a double logarithmic plot. As being evident, the power-law relation seems suitable for the fit since good R^2 are attained. It is found that

$$P_r = \exp(-0.0068E_0 + 10.305)T^{(0.0022E_0-1.2322)}. \quad (2)$$

The relation between E_C and T is shown in Fig. 3(b). Surprisingly, linear relations are apparent so an approximation on $y=ax+b$ could be used to fit the data. Nonlinear fits between E_C and T are also performed (not shown) and the linear dependence of E_C and T is confirmed. Therefore, it could be estimated that

$$E_C = (-0.000\,03E_0 - 0.030\,85)T + (0.0459E_0 + 18.319). \quad (3)$$

The temperature dependences of $\langle A\rangle$, P_r, and E_C shown in Eqs. (1)–(3) are also slightly E_0 dependent. Obviously, small coefficients to E_0 (for the whole range of E_0 used in this study) suggests that at fixed E_0

$$\langle A\rangle \propto T^{-1.1024}, \quad (4)$$

$$P_r \propto T^{-1.2322}, \quad (5)$$

$$(E_{C0} - E_C) \propto T. \tag{6}$$

E_{C0} in Eq. (6) can be viewed as the coercivity at $T \sim 0$ K. However, as $T \rightarrow 0$, thermal energy is low, causing a nonsymmetric hysteresis loop; hence, E_{C0} cannot be meaningfully defined. Here E_{C0} is used for proposing the fit, which is valid for the experimental range in this study.

More importantly, Eqs. (4)–(6) present simple relations for the temperature scaling of ferroelectric hysteresis parameters. It should be noted that there have only been few theoretical treatments to include a temperature term in the dynamic hysteresis scaling of ferromagnetics.[2,3,25] Considering relatively successful applications of the treatments to E- and f-dependent ferroelectric hysteresis,[2–5] it would be worthwhile to compare our experimental results with the theoretically derived scaling. Theoretical scaling relations have been proposed as $\langle A \rangle \propto T^{-\gamma}$, with γ being 0.7, 1.18, and 1.98 for continuum three-dimensional (3D) $((\Phi^2)^2$, two-dimensional, and 3D Ising models, respectively.[2,3,25] An explanation for the variation may come from the different polarization-interaction terms as considered in these models. It could be seen that our experimentally obtained temperature scaling of $\langle A \rangle$ (with $\gamma \sim 1.1$) falls between the values obtained from the models. The difference could be attributed to additional contributions from depolarizing effects within the ceramics (arisen from domain walls, grain boundaries, space charges, immobile defects, etc.),[13,14] as compared to physically oversimplified polarization interaction proposed in the theoretical models.[2,3,25]

Furthermore, the relation $E_C \propto (T - T_C)^{-0.35}$ drawn from the 3D $((\Phi^2)^2$ model[2] is significantly different from the linear relation obtained from our study, which further clarifies that the theoretical models cannot be applied to ferroelectric bulk ceramics. This study clearly serves as a survey to show that more improvement of the theoretical approach is needed to predict the scaling behavior in bulk ferroelectric ceramics. Interestingly, different forms of temperature scaling of E_C extracted from the previous experimental data on PZT thin films also indicate dimensional dependence of the coercivity, as reported in previous investigations.[8,26,27]

In approaching the saturation, the hysteresis area can be roughly estimated with $(2P_r)(2E_C)$.[9,18] It is also interesting to check if the product of P_r and E_C would provide the same scaling law on the T dependence in comparison with $\langle A \rangle$. So, by substituting the E_0 dependence on both E_C and P_r [Eqs. (2) and (3)], it is found that

$$\begin{aligned}(2E_C)(2P_r) = 4[&(-0.000\,03E_0 - 0.030\,85)T + (0.0459E_0 \\ &+ 18.319)] \times [\exp(-0.0068E_0 \\ &+ 10.305)T^{(0.0022E_0 - 1.2322)}].\end{aligned} \tag{7}$$

Since all coefficients to E_0 are small, by taking an approximation that E_0 is fixed (or not very high), the $(2P_r) \times (2E_C)$ reduces to

$$(2E_C)(2P_r) \approx 4(9.2 \times 10^2 T^{-0.2322} + 5.5 \times 10^5 T^{-1.2322}). \tag{8}$$

As can be seen, the term $T^{-1.2322}$ strongly decays in temperature than the term $T^{-0.2322}$, but $T^{-1.2322}$ has a much larger coefficient. However, by substituting all temperatures used in this study, it is found that $T^{-1.2322}$ should be a principal term. Therefore, the scaling of "area" in this way on the temperature should have the exponent γ closer to -1.2322. In comparison with those extracted from the $\ln\langle A \rangle$ and $\ln T$ plot (in which the exponent γ has a value of -1.1024), these two scaling methods seem to agree. So once the scaling of area to the temperature is found, it is possible to guess how the E_C would scale with T if the scaling relation between P_r and T is known or vice versa. Similarly, a scaling of area to frequency has also been reported in a previous investigation.[28]

In summary, the power-law temperature scaling relations have been found for hystersis area $\langle A \rangle$ and remnant polarization P_r, while the coercivity E_C scales linearly with temperature. The three temperature scaling relations are also field dependent. At fixed E_0, the scaling relations take the forms of $\langle A \rangle \propto T^{-1.1024}$, $P_r \propto T^{-1.2322}$, and $(E_{C0} - E_C) \propto T$. Furthermore, the product of P_r and E_C also provides the same scaling law on the T dependence in comparison with $\langle A \rangle$.

Financial support from the Thailand Research Fund (TRF) and the Commission on Higher Education (CHE) are gratefully acknowledged.

[1] K. Uchino, *Ferroelectric Devices* (Dekker, New York, 2000).
[2] M. Rao, H. R. Krishnamurthy, and R. Pandit, Phys. Rev. B **42**, 856 (1990).
[3] M. Acharyya and B. K. Chakrabarti, Phys. Rev. B **52**, 6560 (1995).
[4] L.-F. Wang and J.-M. Liu, J. Appl. Phys. **98**, 064106 (2005).
[5] J.-M. Liu, H. L. W. Chan, C. L. Choy, and C. K. Ong, Phys. Rev. B **65**, 014416 (2001).
[6] Q. Jiang, H. N. Yang, and G. C. Wang, Phys. Rev. B **52**, 14911 (1995).
[7] Y.-H. Kim and J.-J. Kim, Phys. Rev. B **55**, R11933 (1997).
[8] J. S. Suen and J. L. Erskine, Phys. Rev. Lett. **78**, 3567 (1997).
[9] J.-M. Liu, H. P. Li, C. K. Ong, and L. C. Lim, J. Appl. Phys. **86**, 5198 (1999).
[10] B. Pan, H. Yu, D. Wu, X. H. Zhou, and J.-M. Liu, Appl. Phys. Lett. **83**, 1406 (2003).
[11] J.-H. Park, C.-S. Kim, B.-C. Choi, B. K. Moon, J. H. Jeong, and I. W. Kim, Appl. Phys. Lett. **83**, 536 (2003).
[12] J.-M. Liu, B. Pan, H. Yu, and S. T. Zhang, J. Phys.: Condens. Matter **16**, 1189 (2004).
[13] R. Yimnirun, Y. Laosiritaworn, S. Wongsaenmai, and S. Ananta, Appl. Phys. Lett. **89**, 162901 (2006).
[14] R. Yimnirun, S. Wongsaenmai, S. Ananta, and Y. Laosiritaworn, Appl. Phys. Lett. **89**, 242901 (2006).
[15] M. E. Lines and A. M. Glass, *Principles and Applications of Ferroelectrics and Related Materials* (Clarendon, Oxford, 1977).
[16] T. Mihara, H. Watanabe, and C. A. Araujo, Jpn. J. Appl. Phys., Part 1 **33**, 3996 (1994).
[17] Q. Tan, J. Li, and D. Viehland, Appl. Phys. Lett. **75**, 418 (1999).
[18] G. L. Yuan, J.-M. Liu, S. T. Zhang, D. Wu, Y. P. Wang, Z. G. Liu, H. L. W. Chan, and C. L. Choy, Appl. Phys. Lett. **84**, 954 (2004).
[19] B. S. Li, G. R. Li, Q. R. Yin, Z. G. Zhu, A. L. Ding, and W. W. Cao, J. Phys. D **38**, 1107 (2005).
[20] D. Lin, D. Xiao, J. Zhu, and P. Yu, Appl. Phys. Lett. **88**, 062901 (2006).
[21] W. Chang, A. H. King, and K. Bowman, Appl. Phys. Lett. **88**, 242901 (2006).
[22] S. K. Pandey, O. P. Thakur, A. Kumar, C. Prakash, R. Chatterjee, and T. C. Goel, J. Appl. Phys. **100**, 014104 (2006).
[23] A. Gruverman, O. Auciello, and H. Tokumoto, Annu. Rev. Mater. Sci. **28**, 101 (1998).
[24] K. Lee and S. Baik, Annu. Rev. Mater. Res. **36**, 81 (2006).
[25] M. Rao and R. Pandit, Phys. Rev. B **43**, 3373 (1991).
[26] O. Lohse, D. Bolten, S. Tiedke, T. Schneller, and R. Waser, Proceedings of the IEEE-ISAF 98 (IEEE, Piscataway, NJ, 1998), Vol. 1, p. 27.
[27] H. Maiwa and N. Ichinose, Ferroelectrics **293**, 89 (2003).
[28] J.-M. Liu, W. M. Wang, Z. G. Liu, H. L. Chan, and C. L. Choy, Appl. Phys. A: Mater. Sci. Process. **75**, 507 (2002).

Dynamic hysteresis and scaling behavior of hard lead zirconate titanate bulk ceramics

R. Yimnirun,[a] R. Wongmaneerung, S. Wongsaenmai, A. Ngamjarurojana, S. Ananta, and Y. Laosiritaworn
Department of Physics, Faculty of Science, Chiang Mai University, Chiang Mai 50200, Thailand

(Received 20 November 2006; accepted 9 February 2007; published online 14 March 2007)

The scaling relation of ferroelectric hysteresis area $\langle A \rangle$ against frequency f and field amplitude E_0 for the saturated loops of the hard lead zirconate titanate bulk ceramic takes the form of $\langle A \rangle \propto f^{-0.28} E_0^{0.89}$, while that for the minor loops takes the form of $\langle A \rangle \propto f^{-0.43} E_0^{3.19}$. In both cases, the scaling relations are similar to those of its soft counterpart. This indicates that the dynamic behaviors and scaling relations in bulk ceramics are mainly governed by the domain states and structures, while the distinct types of complex defects contribute mainly to the difference in the coercive field observed in hard and soft ceramics. © *2007 American Institute of Physics*.
[DOI: 10.1063/1.2713769]

Lead zirconate titanate [$Pb(Zr_{1-x}Ti_x)O_3$ or (PZT)] ceramics are among the lead-based complex perovskites that have been investigated extensively both from academic and commercial viewpoints with various applications.[1,2] However, PZT ceramics are usually modified with dopants.[3,4] Generally, donor (higher-valency) additives induce "soft" piezoelectric behaviors with higher dielectric and piezoelectric activities, while acceptor (lower-valency) additives result in "hard" piezoelectric behaviors.[1–4]

In many applications, the dynamic hysteresis, i.e., hysteresis area $\langle A \rangle$ as a function of the field amplitude E_0 and frequency f, has become an important consideration.[1–5] Hence, there have been reports on the scaling behavior of the dynamic hysteresis in ferromagnetic and ferroelectric thin films.[6–13] Many theoretical studies have been focused on the scaling law,

$$\langle A \rangle \propto f^{\alpha} E_0^{\beta} \tag{1}$$

(where α and β are exponents that depend on the dimensionality and symmetry of the system), of hysteresis curves in polarization systems.[6–8] Earlier investigations[6–8,13] have reported the scaling relations for the high-f region with α and β values, respectively, of −1 and 2 for $(\Phi^2)^2$ and $(\Phi^2)^3$ models and of −0.33 and 3 for a PZT thin film. We also reported the scaling relation for soft PZT bulk ceramics with α and β values, respectively, of −0.25 and 1 for saturated loops.[14] Interestingly, the scaling form for the minor loops is identical to that of the PZT thin film. The difference in the scaling relations has been attributed to the different domain dynamics.[14] Generally, the domain dynamics differs depending on the composition and the doping type.[15,16] In this point of view, the domain dynamics in hard and soft PZT ceramics, which contain distinct types of complex defects, should be very different.[16] Since our earlier work has already shown unique scaling relations for the soft PZT bulk ceramics,[14] it will be of interest to investigate the scaling behavior of the hard PZT bulk ceramic, as the direct comparison will help extracting roles of complex defects to the dynamic hysteresis behavior. Thus, we present in this letter the results on the scaling behaviors of the dynamic hysteresis of a hard PZT bulk ceramic. As will be seen, the dynamic hysteresis and scaling behaviors of the hard ceramic are surprisingly very similar to those of the soft one.

The dynamic hysteresis (P-E) loops of commercial hard PZT ceramic disks (APC-840, APC International, Ltd., USA) with a diameter of 8 mm and a thickness of 1 mm were characterized at room temperature (298 K) by using a modified Sawyer-Tower circuit with f covering from 1 to 100 Hz and E_0 from 0 to 40 kV/cm. The electric field was applied to a sample by a high voltage ac amplifier (Trek 610D) with the input sinusoidal signal from a function generator (HP 3310A). The P-E loops were recorded by a digital oscilloscope (HP 54645A, 100 MHz). Each loop was obtained after 20 sampling cycles to average out the noise deformation. The hysteresis loop obtained was very consistent with that obtained by a standardized ferroelectric testing unit, RT66A (Radiant Technologies Inc., NM), which ensures the reliability of the measurements. It should be noted that the exact compositional formulation for APC-840 is proprietary to APC International, Ltd., but our elemental analysis showed multiple lower valent substituents, such as Na, Ni, Co, and Ga, which are known to produce hard properties through the formation of complex defects.[1,2,4,15,16]

The hysteresis loops of unpoled samples at different f but fixed E_0 (40 kV/cm) and at different E_0 but fixed f (20 Hz) are shown in Fig. 1. The loop area $\langle A \rangle$, remanent polarization (P_r), and coercive field (E_c) decrease with an increase of frequency, as shown in Fig. 1(a). The dependence of the hysteresis loop on E_0 is depicted in Fig. 1(b). For small fields (10 and 15 kV/cm), the loops do not saturate. With further increase in E_0, $\langle A \rangle$, P_r, and E_c increase until a well saturated loop is achieved. Similar observations have been reported in thin films and ceramics.[8,10,13,14]

To investigate the scaling behavior for unpoled hard PZT bulk ceramics, we followed the scaling relation reported earlier for soft PZT bulk ceramics in the form of $\langle A \rangle \propto f^{-0.25} E_0$.[14] The data are shown in Fig. 2 and the solid line represents the fitting. Surprisingly, it is revealed that the high E-field (saturated loops) data can be fitted reasonably well ($R^2 \sim 0.97$) with the scaling relation obtained experimentally for the soft PZT bulk ceramics. However, some deviation is still ob-

[a]Author to whom correspondence should be addressed; electronic mail: rattikornyimnirun@yahoo.com

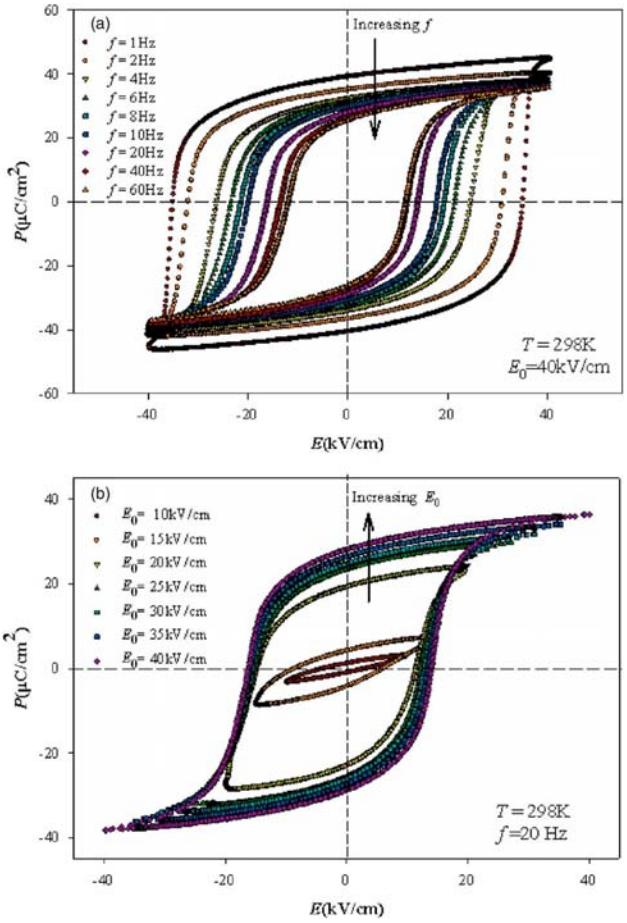

FIG. 1. (Color online) Hysteresis loops for hard PZT bulk ceramic (a) at various f and E_0=40 kV/cm and (b) at various E_0 and f=20 Hz.

served, particularly for low E-field (minor loops) data. This was also the case for the soft PZT bulk ceramics, as reported earlier,[14] in which the different scaling relations were obtained for the saturated and minor loops. Apparently, a similar situation is also observed in the hard PZT bulk ceramics.

Attempt to obtain better scaling can be done by fitting the data with $\langle A\rangle \propto f^m E_0^n$, where m and n are exponents to be determined directly from the experimental data. By plotting $\langle A\rangle$ against f at fixed E_0, one obtains the exponent m. On the

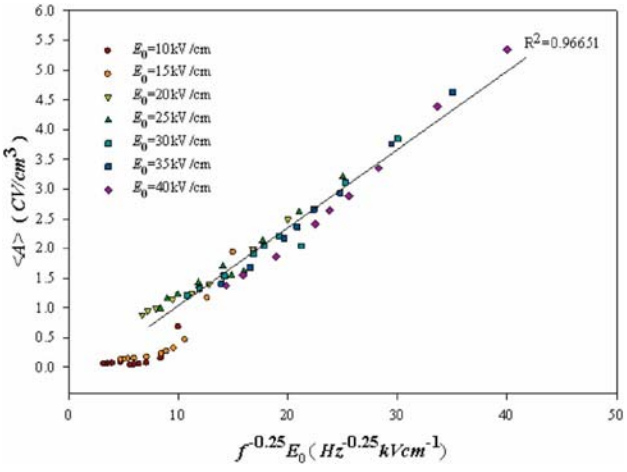

FIG. 2. (Color online) Scaling of hysteresis area $\langle A\rangle$ against $f^{-0.25}E_0$ for hard PZT bulk ceramic.

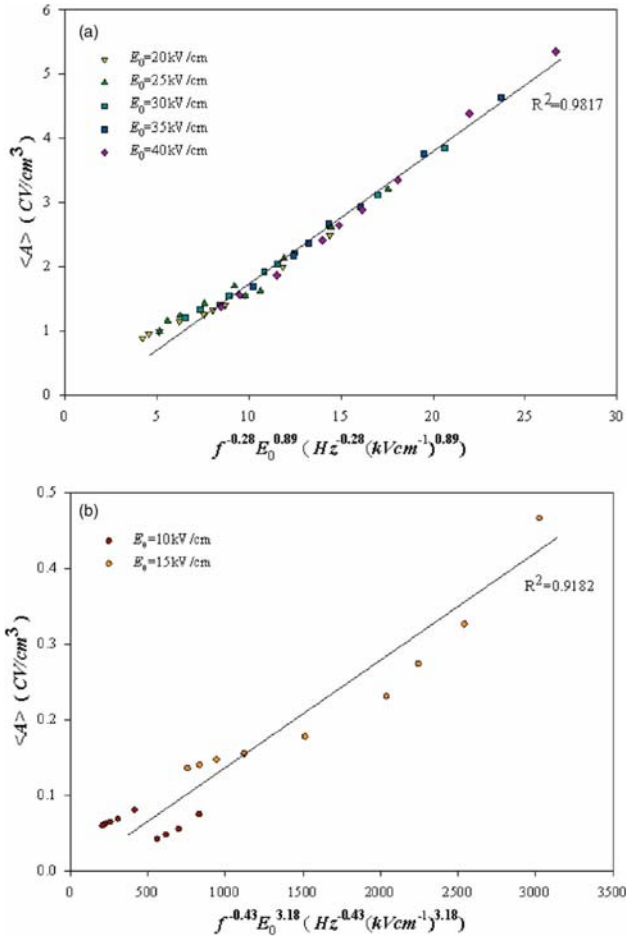

FIG. 3. (Color online) Scaling of hysteresis for hard PZT bulk ceramic. (a) Area $\langle A\rangle$ against $f^{-0.28}E_0^{0.89}$ for the saturated loops; (b) area $\langle A\rangle$ against $f^{-0.43}E_0^{3.19}$ for the minor loops.

other hand, the exponent n can be obtained from plotting $\langle A\rangle$ against E_0 at fixed f. By least-squares-fitting method, for the high E-field data (saturated loops) the exponents $m=-0.28\pm0.01$ and $n=0.89\pm0.05$ were obtained. As plotted in Fig. 3(a), it is revealed that the high E-field data can be fitted only slightly better ($R^2\sim0.98$), within the measured uncertainty, by

$$\langle A\rangle \propto f^{-0.28}E_0^{0.89}. \tag{2}$$

Furthermore, the exponents $m=-0.43\pm0.08$ and $n=3.19\pm0.56$ were obtained and fitted reasonably well ($R^2\sim0.92$) for the minor loop data, as plotted in Fig. 3(b). Therefore, the scaling relation for minor loops of hard PZT bulk ceramic takes the form of

$$\langle A\rangle \propto f^{-0.43}E_0^{3.19}. \tag{3}$$

The scaling relation obtained in Eq. (2) for the saturated loops of the hard PZT bulk ceramic indicates that $\langle A\rangle$ decays more slowly with f and grows more slowly with E_0 than that theoretically predicted and that observed in the PZT thin film, as listed in Table I and discussed in an earlier publication.[14]

As listed in Table I, it is even more interesting to observe that the scaling behaviors for the hard PZT bulk ceramic are to some extent similar to those of the soft counterpart. By a direct comparison, the exponents m and n for the two ceram-

TABLE I. Dynamic scaling exponents for different systems [refer to Eq. (1)].

System	α	β	References
$(\Phi^2)^2$ and $(\Phi^2)^3$ model	−1	2	6 and 7
1–3 composite	−1	2	17
Nd-doped $Bi_4Ti_3O_{12}$ thin film	−0.66	2	18
SBT thin film	−0.33	2	19
PZT thin film	−0.33	3	13
Soft PZT bulk ceramic			
-Saturated loops	−0.25	1	14
-Minor loops	−0.33	3	14
Hard PZT bulk ceramic			
-Saturated loops	−0.28±0.01	0.89±0.05	This work
-Minor loops	−0.43±0.08	3.19±0.56	This work

ics are not significantly different. As well known, the major difference between the two types of ceramic is the complex defects.[1,3,4,15,16] In the hard PZT, the oxygen vacancies are introduced, are trapped at the domain walls, and then form electric dipoles with the acceptor atoms. These dipoles called complex defects act as pinning points for the domain wall, and the domain wall motion is reduced. The complex defects are absent in the soft PZT ceramics; hence the domain walls can move more easily. Therefore, hard PZT ceramics typically show higher E_C than soft ones. Other dielectric and piezoelectric properties of the two types of ceramics are also significantly different.[1–4,15,16] However, the similar scaling behaviors for the two types of ceramics suggest that though the complex defects contribute greatly to the difference on the electrical properties, they contribute only slightly to the dynamic behaviors. At high fields (saturated loops), one can picture that beyond the critical field, i.e., E_C which is different between the hard and soft ceramics, the dynamic hysteresis behavior of the PZT bulk ceramics is mainly governed by the available domain states for polarization switching, while the contribution the complex defects is very minimal; hence the scaling behavior is nearly similar between the hard and soft PZT ceramics. However, at lower fields (minor loops), the complex defects still play limited roles in controlling the dynamic behavior, as can be observed from the relatively larger differences in the values of m and n between the soft and hard PZT ceramics.

More importantly, all these observations suggest that bulk PZT ceramics with similar domain structures should have very comparable dynamic hysteresis and scaling behavior. As also listed in Table I, it is interesting to observe that models and thin films of different materials, which contain similar domain structures, show comparable scaling behaviors (with only a slight difference in exponents m and n). It could be stated that the dynamic hysteresis (hence the scaling behavior) is mainly controlled by available domain states and polarization switching mechanism. Therefore, the scaling relations obtained theoretically and experimentally from models, thin films, and bulks with distinct types of domain structures and mechanisms should be noticeably different (hence different universality classes among them), as shown in Table I. Our opinion on the contribution of the domain states in controlling the dynamic hysteresis behavior may be strengthened by a further study of the domain states in different materials, particularly in soft and hard PZT ceramics. Previous transmission electron microscopy studies have already shown fine "wavy" domains in hard PZT, while irregular domain morphologies have been reported in soft PZT.[20–22] Thus, giving the complexity of the dopant types and concentrations in the commercial hard and soft PZT ceramics, it may be too complicated to evaluate the domain state contribution to the dynamic behavior in these ceramics. It is more suitable to compare the domain states in undoped PZT and single-element soft- and hard-doped PZT ceramics.[15,23]

In summary, the scaling relation for the saturated hysteresis loops of the hard PZT ceramic takes the form of $\langle A\rangle \propto f^{-0.28}E_0^{0.89}$, while that for the minor loops takes the form of $\langle A\rangle \propto f^{-0.43}E_0^{3.19}$. The two scaling relations are very similar to those of soft PZT bulk ceramics, suggesting that the scaling behaviors of the two types of bulk ceramics are in the same universality class.

This work was supported by the Thailand Research Fund (TRF), Commission on Higher Education (CHE), and Faculty of Science and Graduate School of Chiang Mai University.

[1] B. Jaffe, W. R. Cook, and H. Jaffe, *Piezoelectric Ceramics* (Academic, New York, 1971), p. 271.
[2] Y. H. Xu, *Ferroelectric Materials and Their Applications* (North Holland, Los Angeles, 1991), p. 121.
[3] K. Uchino, *Ferroelectric Devices* (Dekker, New York, 2000), p. 145.
[4] A. J. Moulson and J. M. Herbert, *Electroceramics* (Wiley-Interscience, New York, 2003), p. 358.
[5] J. F. Scott, Ferroelectr. Rev. **1**, 1 (1998).
[6] M. Rao, H. R. Krishnamurthy, and R. Pandit, Phys. Rev. B **42**, 856 (1990).
[7] M. Acharyya and B. K. Chakrabarti, Phys. Rev. B **52**, 6560 (1995).
[8] J.-M. Liu, H. L. W. Chan, C. L. Choy, Y. Y. Zhu, S. N. Zhu, Z. G. Liu, and N. B. Ming, Appl. Phys. Lett. **79**, 236 (2001).
[9] Q. Jiang, H. N. Yang, and G. C. Wang, Phys. Rev. B **52**, 14911 (1995).
[10] B. Pan, H. Yu, D. Wu, X. H. Zhou, and J.-M. Liu, Appl. Phys. Lett. **83**, 1406 (2003).
[11] Y.-H. Kim and J.-J. Kim, Phys. Rev. B **55**, R11933 (1997).
[12] J.-H. Park, C.-S. Kim, B.-C. Choi, B. K. Moon, J. H. Jeong, and I. W. Kim, Appl. Phys. Lett. **83**, 536 (2003).
[13] J.-M. Liu, H. L. W. Chan, and C. L. Choy, Mater. Lett. **52**, 213 (2002).
[14] R. Yimnirun, Y. Laosiritaworn, S. Wongsaenmai, and S. Ananta, Appl. Phys. Lett. **89**, 162901 (2006).
[15] Q. Tan, J. Li, and D. Viehland, Appl. Phys. Lett. **75**, 418 (1999).
[16] W. Chang, A. H. King, and K. J. Bowman, Appl. Phys. Lett. **88**, 242901 (2006).
[17] B. Pan, Y. Yang, L. C. Yu, J. M. Liu, K. Li, Z. G. Liu, and H. L. W. Chan, Mater. Sci. Eng., B **B99**, 179 (2005).
[18] J.-M. Liu, B. Pan, H. Yu, and S. T. Zhang, J. Phys.: Condens. Matter **16**, 1189 (2004).
[19] J.-M. Liu, B. Pan, K. F. Wang, and H. Yu, Ceram. Int. **30**, 1471 (2004).
[20] Q. Tan, Z. Xu, J. F. Li, and D. Viehland, J. Appl. Phys. **80**, 5866 (1996).
[21] J. F. Li, X. H. Dai, A. Chow, and D. Viehland, J. Mater. Res. **10**, 926 (1995).
[22] W. Cao and C. A. Randall, J. Phys. Chem. Solids **37**, 1499 (1996).
[23] T. Granzow, E. Suvaci, H. Kungl, and M. J. Hoffmann, Appl. Phys. Lett. **89**, 262908 (2006).

Available online at www.sciencedirect.com
ScienceDirect
Materials Letters 61 (2007) 2426–2429
materials letters
www.elsevier.com/locate/matlet

Effects of calcination conditions on phase formation and particle size of indium niobate nanopowders synthesized by the solid-state reaction

S. Wongsaenmai, R. Yimnirun, S. Ananta *

Department of Physics, Faculty of Science, Chiang Mai University, Chiang Mai 50200, Thailand

Received 17 March 2006; accepted 13 September 2006
Available online 2 October 2006

Abstract

A wolframite-type phase of indium niobate, $InNbO_4$, has been synthesized by a solid-state reaction via a rapid vibro-milling technique. The formation of the $InNbO_4$ phase in the calcined powders has been investigated as a function of calcination conditions by TG–DTA and XRD techniques. Morphology, particle size and chemical composition have been determined via a combination of SEM and EDX techniques. It has been found that single-phase $InNbO_4$ powders have been obtained successfully at the calcination condition of 950 °C for 2 h with heating/cooling rates of 30 °C/min. Higher temperatures and longer dwell times clearly favoured particle growth and the formation of large and hard agglomerates.

Keywords: Indium niobate; $InNbO_4$; Calcination; Phase formation; Powders–solid-state reaction

1. Introduction

Earlier works concerning the wolframite-type indium niobate ($InNbO_4$, IN) have been directed towards determining low-temperature dielectric, luminescent and photocatalytic properties [1–3]. Recently, this compound is also a potential material for the development of photocatalytic systems capable of splitting water into H_2 and O_2 under visible light irradiation [4,5]. Moreover, it is well established as a key precursor for the partially successful preparation of single-phase ferroelectric perovskite lead indium niobate $Pb(In_{1/2}Nb_{1/2})O_3$ (PIN)-based ceramics, which is becoming increasingly important for actuator, transducer and ultrasonic motor applications [6].

There has been a great deal of interest in the preparation of single-phase perovskite PIN powders as well as in the phase transition, ordering behaviour and electrical properties of PIN-based ceramics [7–11]. In general, the constituents In_2O_3 and Nb_2O_5 are first mixed and reacted together to form indium niobate ($InNbO_4$), prior to mixing and reacting with PbO in the second step of calcination at elevated temperature. Interestingly, this mixed oxide route has been employed with minor modifications in the synthesis of $InNbO_4$ itself [8–11]. However, powders prepared by a mixed oxide route have spatial fluctuations in their compositions. The extent of the fluctuations depends on the characteristics of the starting powders as well as on the processing schedule. Generally, the mixed oxide method involves the heating of a mixture of indium oxide and niobium oxide above 1000 °C for long times *i.e.* 4 h [7,8], 12 h [4], 24 h [9–11] and 48 h [3,5]. The optimization of calcination conditions used in the mixed oxide process, however, has not received detailed attention, and the effects of applied dwell time and heating/cooling rates have not yet been studied extensively.

Therefore, the main purpose of this work is to explore a simple mixed oxide synthetic route for the production of $InNbO_4$ powders via a rapid vibro-milling technique and to perform a systematic study of the reaction between the starting indium oxide and niobium oxide precursors. The phase formation and morphology of the powders calcined at various conditions will be studied and discussed.

2. Experimental procedure

The starting materials were commercially available indium oxide, In_2O_3 (JCPDS file number 71-2195) and niobium oxide, Nb_2O_5 (JCPDS file number 30-873) (Aldrich, 99.9% purity). The two oxide powders exhibited an average particle size in the range of 1.0–3.0 μm. $InNbO_4$ powders were synthesized by the

* Corresponding author. Tel.: +66 53 943367; fax: +66 53 943445.
E-mail address: Supon@chiangmai.ac.th (S. Ananta).

0167-577X/$ - see front matter © 2006 Elsevier B.V. All rights reserved.
doi:10.1016/j.matlet.2006.09.028

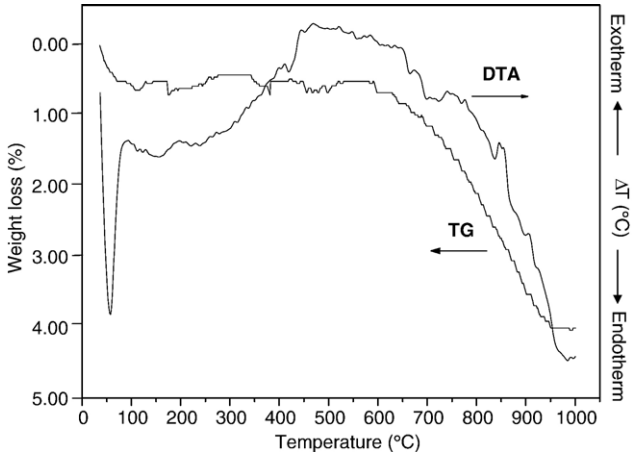

Fig. 1. TG–DTA curves for the mixture of In_2O_3–Nb_2O_5 powder.

solid-state reaction of thoroughly ground mixtures of In_2O_3 and Nb_2O_5 powders that were milled in the required stoichiometric ratio. Instead of employing a ball-milling procedure [7,11], a McCrone vibro-milling technique was used [12]. In order to combine mixing capacity with a significant time saving, the milling operation was carried out for 0.5 h with corundum cylindrical media in isopropyl alcohol (IPA). After drying at 120 °C for 2 h, the reaction of the uncalcined powders taking place during heat treatment was investigated by themogravimetric and differential thermal analysis (TG–DTA, Shimadzu), using a heating rate of 10 °C/min in air from room temperature up to 1000 °C. Based on the TG–DTA results, the mixture was calcined in air at various conditions in a closed alumina crucible, in order to investigate the formation of indium niobate.

Calcined powders were subsequently examined by room temperature X-ray diffraction (XRD; Siemens-D500 diffractometer), using Ni-filtered CuK_α radiation to identify the phases formed and optimum calcination conditions for the formation of $InNbO_4$ powders. Powder morphologies and particle sizes were

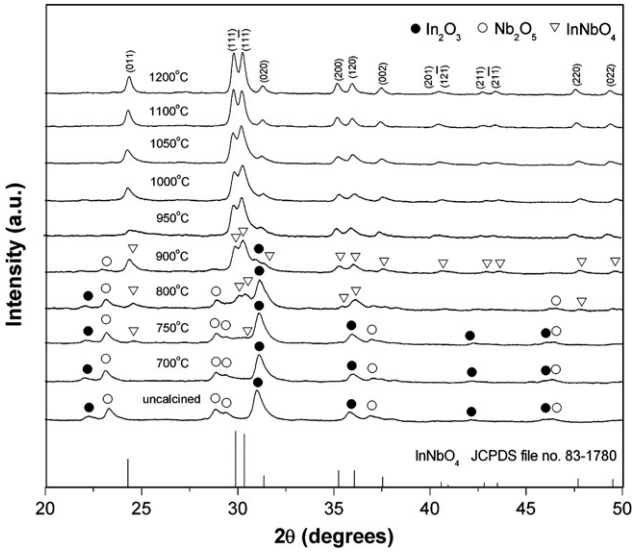

Fig. 2. XRD patterns of IN powders calcined at various temperatures for 2 h with heating/cooling rates of 10 °C/min.

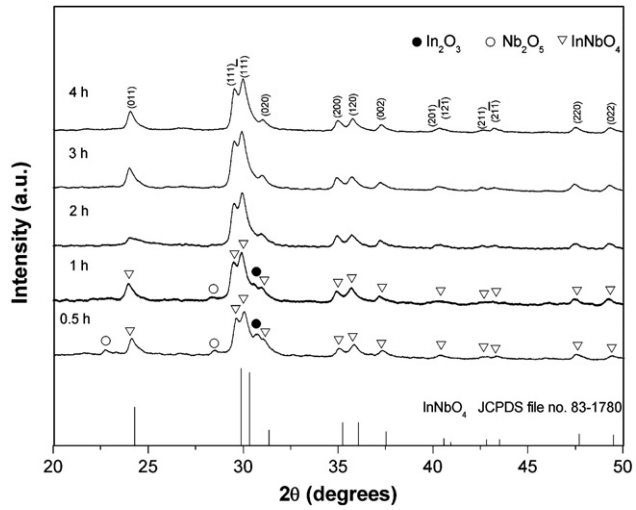

Fig. 3. XRD patterns of IN powders calcined at 950 °C with heating/cooling rates of 10 °C/min for various dwell times.

directly imaged, using scanning electron microscopy (SEM; JEOL JSM-840A). The chemical compositions of the phase formed were elucidated by an energy-dispersive X-ray (EDX) analyzer with an ultra-thin window. EDX spectra were quantified with the virtual standard peaks supplied with the Oxford Instruments eXL software.

3. Results and discussion

The TG–DTA simultaneous analysis of a powder mixed in the stoichiometric proportion of $InNbO_4$ is displayed in Fig. 1. The TG curve shows two distinct weight losses. In the temperature range from room temperature to ~150 °C, both exothermic and endothermic peaks are observed in the DTA curve, in consistent with the first weight loss. These observations can be attributed to the decomposition of the organic species (*i.e.* polyethylene milling jar, rubber gloves, skin, etc.) from the milling process [12]. Increasing the temperature up to ~1000 °C, the solid-state reaction occurred between In_2O_3 and Nb_2O_5 [7,11]. The broad exotherm in the DTA curve represents that reaction, which has a

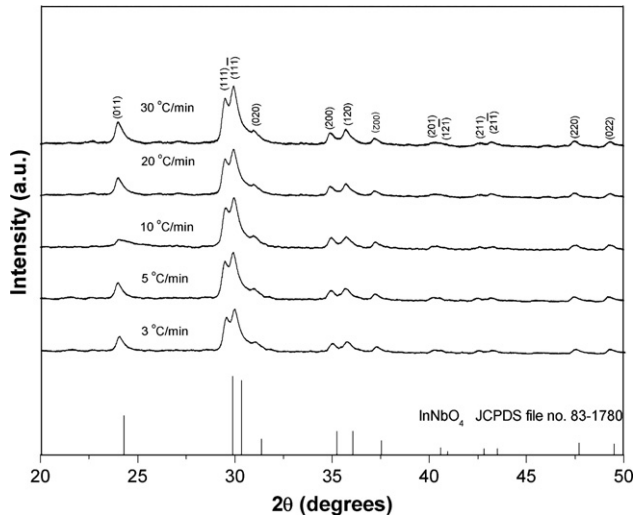

Fig. 4. XRD patterns of IN powders calcined at 950 °C for 2 h with various heating/cooling rates.

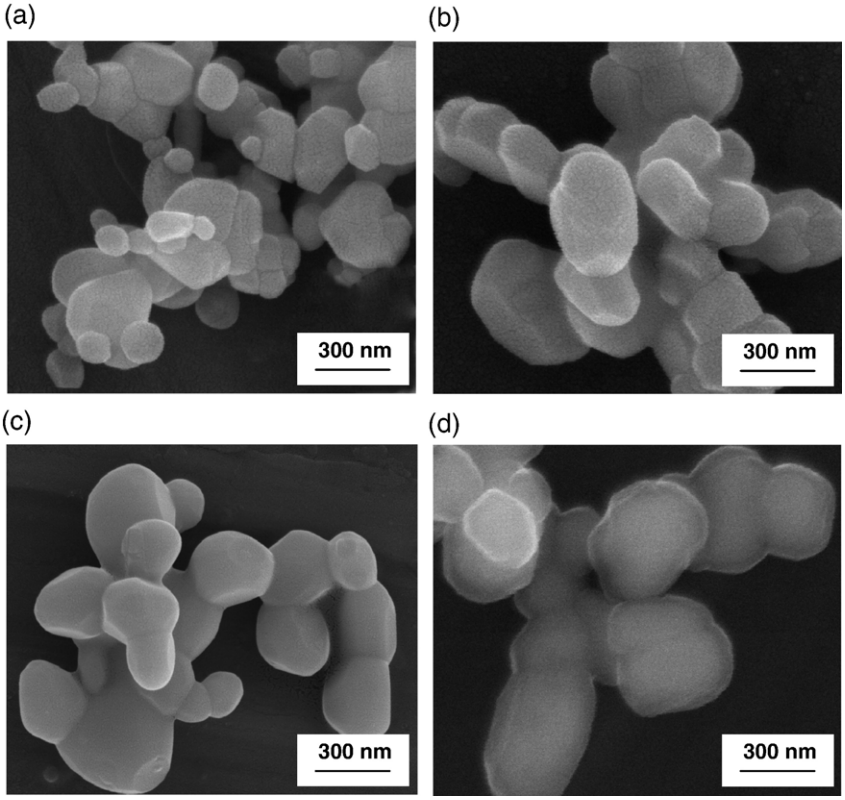

Fig. 5. SEM micrographs of the IN powders calcined at (a) 950 °C for 2 h, (b) 950 °C for 4 h, (c) 1200 °C for 2 h with heating/cooling rates of 10 °C/min, and at (d) 950 °C for 2 h with heating/cooling rates of 30 °C/min.

maximum at ~500 °C. This is supported by a large fall in sample weight over the same temperature range. Although the DTA curve shows that there are other small peaks at ~750, 850 and 900 °C, however, it is to be noted that there is no obvious interpretation of these peaks. These data were used to define the range of calcination temperatures for XRD investigation between 700 and 1200 °C.

To further study the phase development with increasing calcination temperature in the powders, they were calcined for 2 h in air at various temperatures, up to 1200 °C, followed by phase analysis using XRD. As shown in Fig. 2, for the uncalcined powders and the powders calcined at 700 °C, only X-ray peaks of precursors In_2O_3 (●) and Nb_2O_5 (○), which could be matched with JCPDS file numbers 71-2195 [13] and 30-0873 [14], respectively, are present, indicating that no reaction had yet been triggered during the milling or low firing processes. It is seen that fine $InNbO_4$ crystallites (▽) were developed in the powders at a calcination temperature as low as 750 °C, accompanied with In_2O_3 and Nb_2O_5 as separated phases. This observation agrees well with those derived from the TG–DTA results. As the temperature increased to 900 °C, the intensity of the $InNbO_4$ peaks was further enhanced and became the predominant phase. Upon calcination at 950 °C, an essentially monophasic of $InNbO_4$ phase is obtained. This $InNbO_4$ phase was indexable according to a monoclinic wolframite-type structure with lattice parameters a=514.40 pm, b=577.09 pm, c=483.55 pm and β=91.13°, space group *P2/a* (no. 13), in consistent with JCPDS file numbers 83-1780 [15] and literature [2,4]. This study also shows that monoclinic $InNbO_4$ is the only detectable phase in the powders, after calcination in the range of 950–1200 °C. The variation of the intensity ratio between the two major peaks (111) and ($11\bar{1}$) at $2\theta \sim 29$–31° could be attributed mainly to the expansion of the NbO_6 volume similar with those observed in other ABO_4 systems [2,4]. In the structure of $InNbO_4$, there are two kinds of octahedron, InO_6 and NbO_6. The InO_6 octahedron connects to each other to form a zigzag chain by sharing edges. These chains are connected through NbO_6 octahedron to form the three-dimensional network [5,16]. It is believed that the InO_6 chains are highly distorted because they must accommodate the strain of the defect, which probably leads to lattice rotation [5].

In earlier works [3,7,9], long heat treatments at ~1000–1200 °C for at least 4 h were proposed for the formation of $InNbO_4$ by a conventional mixed oxide synthetic route, although no details on phase formation were provided. However, in the present study, it was found that, except the fluctuation of the intensity ratio between the (111) and ($11\bar{1}$) peaks, there are no significant differences between the powders calcined at 950 to 1200 °C with dwell time of only 2 h, as shown in Fig. 2. This observation would clearly suggest the advantages of a rapid vibro-milling technique used in the present study.

Apart from the calcination temperature, the effect of dwell time was also found to be quite significant. From Fig. 3, it can be seen that the single-phase of $InNbO_4$ (yield of 100% within the limitations of the

Table 1
Particle size range of $InNbO_4$ powders calcined at various conditions

Calcination conditions			Estimated particle size range (±10 nm)
Temperature (°C)	Dwell time (h)	Rates (°C/min)	
950	2	3	150–550
950	2	10	150–350
950	2	30	100–350
950	3	10	300–450
950	4	10	300–700
1000	2	10	200–500
1100	2	10	250–600
1200	2	10	350–700

XRD technique) was found to be possible in powders calcined at 950 °C with dwell time of 2 h or more. The appearance of In_2O_3 and Nb_2O_5 phases indicated that full crystallization has not occurred at relatively short calcination times. The observation that the dwell time effect may also play an important role in obtaining a single-phase wolframite product is also consistent with other similar systems [12,17]. It is also very interesting to see that the on-set firing time is approximately 2–22 h shorter than those reported earlier with a conventional ball-milling method [7–11]. The difference could be attributed to the effectiveness of vibro-milling and a carefully optimized reaction. Most importantly, this study suggests that a rapid vibro-milling method can significantly lower the optimum calcination temperature and dwell time for the formation of single-phase $InNbO_4$ powders.

In the present study, an attempt was also made to calcine $InNbO_4$ powders under various heating/cooling rates. In this connection, it is shown that for the powders calcined at 950 °C for 2 h, the yield of $InNbO_4$ phase did not vary significantly with different heating/cooling rates, ranging from 3 to 30 °C/min (Fig. 4). The observation that faster heating/cooling rates are required for the mixtures containing low-melting point oxide constituent (In_2O_3), is in good agreement with early results reported in other similar systems [18,19].

Based on the TG–DTA and XRD data, it may be concluded that, over a wide range of calcination conditions, single-phase $InNbO_4$ cannot be straightforwardly formed via a solid-state mixed oxide synthetic route, unless a careful design of calcination condition is performed. It is well documented that powders prepared by a conventional mixed oxide method have spatial fluctuations in their compositions. The extent of the fluctuation depends on the characteristics of the starting powders as well as the processing schedules [12,17]. It is rather surprising that no evidence of the monoclinic *P2/c* (13) of $InNbO_4$ [20] was found in this study, nor was there any indication of the one with *P2/a* (13) reported by Brixner and Chen [2] being present. The experimental work carried out here suggests that the optimal calcination conditions for single-phase $InNbO_4$ (with impurities undetected by XRD technique) is 950 °C for 2 h with heating/cooling rates as fast as 30 °C/min. Moreover, the formation temperature and dwell time for the production of $InNbO_4$ powders observed in this work are also lower than those reported earlier [8–11]. This clearly emphasizes the advantages of a combination between a rapid vibro-milling technique and a carefully optimized reaction.

The morphological evolution during calcination was investigated by scanning electron microscopy (SEM). Micrographs of $InNbO_4$ powders calcined at various temperatures, dwell times and heating/cooling rates are illustrated in Fig. 5. The influence of calcination conditions on particle size is also given in Table 1. After calcinations at 950 to 1200 °C, the powders have similar morphology. In general, the particles are agglomerated and irregular in shape, with a substantial variation in particle size, particularly in samples calcined at high temperature (Fig. 5(c)). The results indicate that averaged particle size tends to increase with calcination temperatures and dwell times but seems to decrease with faster heating/cooling rates (Table 1).

The effects of dwell time and heating/cooling rates on the morphology of the calcined powders were also found to be quite significant. As expected, it is seen that longer heat treatment leads to larger particle sizes and hard agglomeration (Fig. 5(a) and (b)). As shown in Fig. 5(a) and (d), as well as in Table 1, by increasing the heating/cooling rates, averaged particle size tends to decrease whilst the degree of agglomeration tends to increase. This observation could be attributed to the mechanism of surface energy reduction of the ultrafine powders, *i.e.* the smaller the powder the higher the specific surface area [21]. This finding is also similar to that in $Mg_4Nb_2O_9$ powders synthesized by Ananta [22]. To the author's knowledge, the present data are the first results for the morphology–calcination relationship of $InNbO_4$ powders prepared by the solid-state reaction. It is also of interest to point out that mass production of single-phase $InNbO_4$ nanopowders with the smallest particle size ~100 nm (estimated from SEM micrographs) can be achieved by employing a simple solid-state reaction combined with a rapid vibro-milling technique. In addition, EDX analysis using a 20 nm probe on a large number of particles of the calcined powders confirms that the chemical composition is $InNbO_4$ powders, in good agreement with the XRD results.

4. Conclusions

The solid-state mixed oxide method via a rapid vibro-milling technique is explored in the preparation of single-phase $InNbO_4$ nanopowders. The calcination temperature, dwell time and heating/cooling rates have been found to show a pronounced effect on phase formation and particle size of the calcined $InNbO_4$ powders. This work demonstrated that the single-phase of indium niobate powders with particle size ranging from 100 to 350 nm can be produced via this technique by using a calcination temperature of 950 °C for 2 h, with heating/cooling rates of 30 °C/min. The resulting $InNbO_4$ powders exhibit similar morphology and variety of agglomerated particle sizes, depending on the calcination conditions.

Acknowledgments

We thank the Thailand Research Fund (TRF), Commission on Higher Education (CHE), Graduate School and Faculty of Science, Chiang Mai University for all the support.

References

[1] J.K. Hulme, Phys. Res. 92 (1953) 504.
[2] L.H. Brixner, H.-Y. Chen, Mater. Res. Bull. 15 (1980) 607.
[3] Z. Zou, J. Ye, H. Arakawa, Chem. Phys. Lett. 332 (2000) 271.
[4] Z. Zou, J. Ye, K. Sayama, H. Arakawa, Nature 414 (2001) 625.
[5] Z. Zou, H. Arakawa, J. Photochem. Photobiol., A Chem. 158 (2003) 145.
[6] A.J. Moulson, J.M. Herbert, Electroceramics, 2nd ed.,Wiley, New York, 2003.
[7] E.F. Alberta, A.S. Bhalla, Ferroelectrics 188 (1996) 95.
[8] E.F. Alberta, A.S. Bhalla, J. Phys. Chem. Solids 63 (2002) 1759.
[9] C. Elissalde, F. Weill, J. Ravez, Mater. Sci. Eng., B, Solid-State Mater. Adv. Technol. 25 (1994) 85.
[10] N. Yasuda, T. Mizuno, Appl. Phys. Lett. 66 (1995) 571.
[11] K.H. Lee, S.B. Lee, H. Kim, Ceram. Int. 30 (2004) 1035.
[12] S. Ananta, Mater. Lett. 58 (2004) 2834.
[13] Powder Diffraction File No. 71-2195. International Centre for Diffraction Data, Newton Square, PA, 2000.
[14] Powder Diffraction File No. 30-873. International Centre for Diffraction Data, Newton Square, PA, 2000.
[15] Powder Diffraction File No. 83-1780. International Centre for Diffraction Data, Newton Square, PA, 2000.
[16] Z. Zou, J. Ye, H. Arakawa, Chem. Phys. Lett. 332 (2000) 271.
[17] S. Ananta, R. Brydson, N.W. Thomas, J. Eur. Ceram. Soc. 19 (1999) 489.
[18] R. Tipakontitikul, S. Ananta, Mater. Lett. 58 (2004) 449.
[19] B.C. Kim, J.H. Lee, J.J. Kim, T. Ikegami, Mater. Lett. 52 (2002) 114.
[20] Liebertz, Acta Crystallogr., B 28 (1972) 3100.
[21] J.S. Reed, Principles of Ceramics Processing, 2nd ed.,Wiley, New York, 1995.
[22] S. Ananta, Mater. Lett. 58 (2004) 2530.

Available online at www.sciencedirect.com
ScienceDirect
Materials Letters 61 (2007) 2822–2826
materials letters
www.elsevier.com/locate/matlet

Effect of vibro-milling time on phase formation and particle size of lead zirconate nanopowders

O. Khamman, W. Chaisan, R. Yimnirun, S. Ananta *

Department of Physics, Faculty of Science, Chiang Mai University, Chiang Mai 50200, Thailand

Received 24 March 2006; accepted 17 October 2006
Available online 13 November 2006

Abstract

A perovskite phase of lead zirconate, $PbZrO_3$, nanopowder was synthesized by a solid-state reaction via a rapid vibro-milling technique. The effect of milling time on the phase formation and particle size of $PbZrO_3$ powder was investigated. Powder samples were characterized using TG–DTA, XRD, SEM and laser diffraction techniques. It was found that an average particle size of 50 nm was achieved at 25 h of vibro-milling after which a higher degree of particle agglomeration was observed upon continuation of milling to 35 h. In addition, by employing an appropriate choice of milling time, a narrow particle size distribution curve was also observed.

Keywords: Lead zirconate; Milling; Nanopowders; Phase formation; Particle size

1. Introduction

Lead zirconate, $PbZrO_3$ (PZ), is one of the antiferroelectric materials which exhibit a perovskite structure. It shows antiferroelectric phase with cubic symmetry at high temperature and undergoes two phase transitions which are close in temperature (~230 °C and 220 °C) upon cooling [1]. The low temperature phase has orthorhombic symmetry with antiparallel shift of Pb ions along the pseudocubic <110>, which results in antiferroelectricity [2]. When combined with other oxides, lead zirconate can form a series of solid solutions such as $Pb(Zr_{1-x},Ti_x)O_3$ (PZT), $(Pb,La)(Zr,Ti)O_3$ (PLZT), $Pb(Fe_{1/3}W_{2/3})O_3$–$PbZrO_3$ (PFW–PZ) and $Pb(Zn_{1/3}Nb_{2/3})O_3$–$PbZrO_3$ (PZN–PZ) [2–4]. These compositions are widely used in ultrasonic transducers, electro-optic devices, nonvolatile memories, microactuators and multilayer capacitors [1–4]. To fabricate them, a fine powder of perovskite phase with a minimal degree of particle agglomeration is needed as the starting material in order to achieve a dense and uniform microstructure at a given sintering temperature. Thus, a crucial focus of powder synthesis in recent years has been the formation of uniform-sized, single morphology particulates ranging in size from nanometer to micrometers [5–8].

The development of a method to produce nanopowders of precise stoichiometry and desired properties is complex, depending on a number of variables such as nature and purity of starting materials, processing history, temperature, etc. To obtain nanosized PZ powders, many investigations have focused on several chemistry-based preparation routes, such as sol–gel [5], homogeneous precipitation [6], hydrothermal reaction [7], oxidant-peroxo method [8], besides the more conventional solid-state reaction of mixed oxides [9]. All these techniques are aimed at reducing the particle size and temperature of preparation of the compound even though they are more involved and complicated in approach than the solid-state reaction. Moreover, high-purity PZ nanopowders are still not available in bulk quantity. The advantage of using mechanical milling for preparation of nanosized powders lies in its ability to produce mass quantities of powders in the solid state using simple equipment and low-cost starting precursors [10]. Although some research has been done in the preparation of PZ powders via a vibro-milling technique [9], to our knowledge a systematic study regarding the influence of milling time on the preparation of PZ powders has not yet been reported.

* Corresponding author. Tel.: +66 53 943367; fax: +66 53 943445.
E-mail address: suponananta@yahoo.com (S. Ananta).

0167-577X/$ - see front matter © 2006 Elsevier B.V. All rights reserved.
doi:10.1016/j.matlet.2006.10.063

Thus, in the present study, the effect of milling time on phase formation, and particle size of lead zirconate powders was investigated in this connection. The potential of the vibro-milling technique as a simple and low-cost method to obtain usable quantities of single-phase lead zirconate powders at low temperature and with nanosized particles was also examined.

2. Experimental procedure

The starting materials were commercially available lead oxide, PbO (JCPDS file number 77-1971) and zirconium oxide, ZrO_2 (JCPDS file number 37-1484) (Fluka, >99% purity). The two oxide powders exhibited an average particle size in the range of 3 to 5 μm. $PbZrO_3$ powder was synthesized by the solid-state reaction of these raw materials. Powder-processing was carried out in a manner similar to that employed in the preparation of other materials, as described previously [10,11]. A vibratory laboratory mill (McCrone Micronizing Mill) powered by a 1/30 HP motor was employed for preparing the stoichiometric $PbZrO_3$ powders. The grinding vessel consists of a 125 ml capacity polypropylene jar fitted with a screw-capped, gasketless, polythene closure. The jar is packed with an ordered array of identical, cylindrical, grinding media of polycrystalline corundum (instead of employing zirconia media under alcohol for 8 h [9]). A total of 48 milling media cylinder with a powder weight of 20 g was kept constant in each batch. The milling operation was carried out in isopropanol inert to the polypropylene jar. Various milling times ranging from 0.5 to 35 h were selected in order to investigate the phase formation characteristic of lead zirconate and the smallest particle size. After drying at 120 °C for 2 h, the reaction of the uncalcined powders taking place during heat treatment was investigated by thermogravimetric and differential thermal analysis techniques (TG–DTA, Shimadzu) at a heating rate of 10 °C/min in air from room temperature up to 1000 °C. Based on the TG–DTA results and literature [9,12], the mixture was calcined at 800 °C (in closed alumina crucible) for 2 h with heating/cooling rates of 10 °C/min.

All powders were subsequently examined by room temperature X-ray diffraction (XRD; Siemens-D500 diffractometer), using Ni-filtered CuK_α radiation to identify the phases formed and optimum milling time for the production of $PbZrO_3$ powders having the smallest particle size. The relative amount of perovskite and secondary phases was determined from XRD patterns of the samples by measuring the major characteristic peak intensities for the perovskite (221) or I_P and secondary (o) phases or I_S. The following qualitative equation was used [10].

$$\text{perovskite phase (wt.\%)} = \frac{I_P}{I_P + I_S} \times 100 \quad (1)$$

The crystalline lattice constants, lattice strain and average particle size were also estimated from XRD patterns [13]. The particle size distributions of the powders were determined by laser diffraction technique (DIAS 1640 laser diffraction spectrometer) with the particle sizes and morphologies of the powders observed by scanning electron microscopy (JEOL JSM-840A SEM). The particle sizes of PZ powders milled at different times obtained from different measuring techniques are provided in Table 1.

3. Results and discussion

The TGA and DTA results for the powders milled at different times are compared and displayed in Fig. 1(a) and (b), respectively. In general, similar thermal characteristics are observed in all cases. In the temperature range from room temperature to ~150 °C, all samples show both exothermic and endothermic peaks in the DTA curves (Fig. 1(b)), which are related to a slight drop in weight loss at the same temperature range. These observations can be attributed to the decomposition of the organic species originating from the milling process [10,11]. Corresponding to the large fall in specimen weight, (~8–9%), the other DTA peaks are detected within ~300 to 450 °C temperature range. However, it is to be noted that there is no obvious interpretation of these peaks, although it is likely to correspond to a phase transformation of ZrO_2 precursor alloyed with PbO precursor suggested by Aoyama et al. [14]. Increasing the temperature up to ~800 °C, the solid-state reaction between lead oxide and zirconium oxide occurs. The broad exothermic characteristics from ~500 to 700 °C in all DTA curves represent that reaction, which is supported by a gradual decrease in sample weight over the same temperature range. The slightly different temperature, intensities and shapes of the thermal peaks of the powders are probably related to the different sizes of the

Table 1
Effect of milling time on the particle size of PZ powders measured by different techniques

Milling time (h)	Perovskite phase (%)	XRD				SEM		Laser scattering	
		A (nm)	*a* (nm)	*b* (nm)	*c* (nm)	*D* (nm)	*P* (nm)	*D* (nm)	*P* (nm)
0.5	93.34	57.39	0.8162	1.1624	0.5814	3800	2410–5000	5280	2840–7650
2	100	42.51	0.8161	1.1611	0.5816	1800	970–2520	1380	1340–5600
5	100	30.73	0.8184	1.1679	0.5846	880	740–950	1380	580–3000
15	100	18.17	0.8238	1.1712	0.5872	300	70–700	720	290–2210
25	100	18.19	0.8241	1.1720	0.5879	180	50–400	180	35–750
35	100	19.34	0.8238	1.1712	0.5872	250	50–420	1540	240–6200

A = Crystallite size.
a, *b*, *c* = Lattice parameters.
D = Average particle size.
P = Particle size distribution or range.

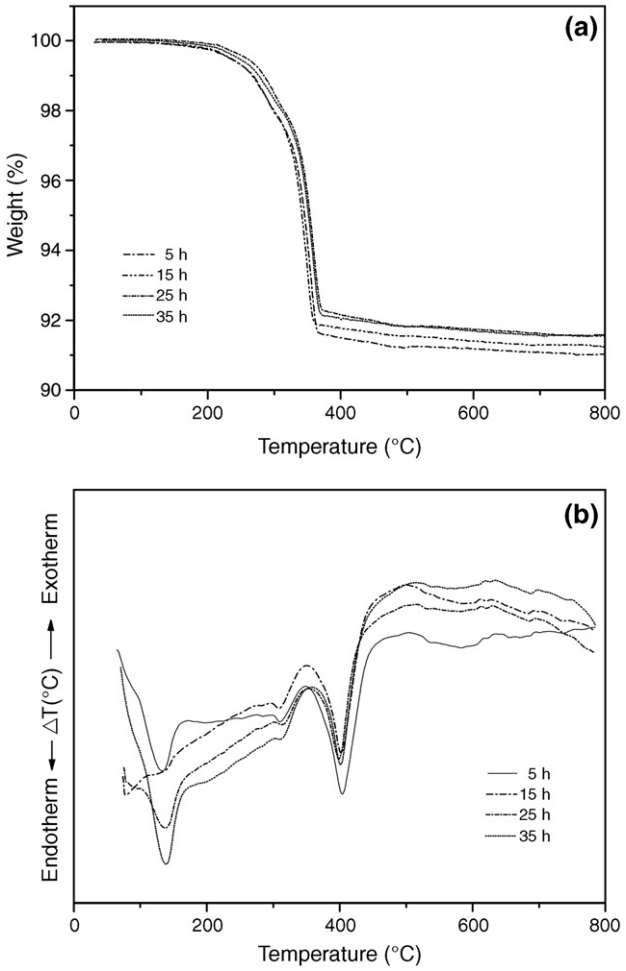

Fig. 1. (a) TGA and (b) DTA analysis of powder mixtures milled at different times.

powders subjected to different milling times and, consequently, caused by the removal of organic species and rearrangement of differently bonded species in the network [2,15].

To further study the effect of milling time on phase formation, each of the powders milled for different times were calcined at 800 °C for 2 h in air, followed by phase analysis using XRD. For the purpose of estimating the concentrations of the phase present, Eq. (1) has been applied to the powder XRD patterns obtained, as given in Table 1. As shown in Fig. 2, for the uncalcined powder subjected to 0.5 h of vibro-milling, only X-ray peaks of precursors PbO (●) and ZrO_2 (○) are present, indicating that no reaction had been initiated during the milling process. However, after calcination, it is seen that the perovskite-type $PbZrO_3$ becomes the predominant phase in the powder milled for 0.5 h, indicating that the reaction has occurred to a considerable extent. It is seen that only traces of unreacted PbO and ZrO_2 precursors have been found along with the PZ parent phase at a milling time of 1.5 h or less. This observation could be attributed mainly to the poor mixing capability under short milling time, similar with another work [10]. With milling time of 2 h or more, it is apparent that a single-phase perovskite PZ (yield of 100% within the limitations of the XRD technique) was found to be possible after the same calcination process was applied.

In general, the strongest reflections found in the majority of these XRD patterns indicate the formation of the lead zirconate, $PbZrO_3$. These can be matched with JCPDS file number 35-0739 for the orthorhombic phase, in space group *P2cb* (no. 32) with cell parameters $a=823.1$ pm, $b=1177.0$ pm and $c=588.1$ pm [16], consistent with other works [6,7]. It should be noted that no evidence for the introduction of impurity due to wear debris from the milling process was observed in any of the calcined powders (within the milling periods of 0.5–35 h), demonstrating the effectiveness of the vibro-milling technique for the production of high-purity PZ nanopowders, without any introduction of excess ZrO_2 [9].

Moreover, it has been observed that with increasing milling time, all diffraction lines broaden, e.g. (261) and (402) peaks, as shown in Fig. 2, an indication of a continuous decrease in particle size and of the introduction of lattice strain. These observations indicate that the prolonged milling treatment affects the particle size and evolution of crystallinity of the phase formed (Table 1), in good agreement with other similar system [10]. For PZ powders, the longer the milling time, the finer the particle size, up to a certain level. The results suggest that the steady state of the vibro-milling is attained at ~25 h of milling. Moreover, it is worthy to note that, in this condition, the mean crystalline size is close to ~50 nm. Also, the relative intensities of the Bragg peaks and the calculated lattice parameters (*b* and *c*) for the powders tend to decrease with the increase of milling time. However, it is well documented that, as Scherrer's analysis provides only a measurement of the extension of the coherently diffracting domains, the particle sizes estimated by this method can be significantly under estimated [17]. In addition to strain, factors such as dislocations, stacking faults, heterogeneities in composition and instrumental broadening can contribute to peak broadening, making it almost impossible to extract a reliable particle size solely from XRD [12,18].

In this connection, scanning electron microcopy was also employed for particle size measurement (Table 1). The morphological evolution of the powders and their corresponding particle size distributions as a function of milling time were also revealed, as illustrated in Fig. 3. At first sight, the morphological characteristic of PZ powders with various milling times is similar for all cases. In general, the particles are agglomerated and basically irregular in shape, with a substantial variation in particle sizes. The powders consist of primary particles nanometers in size. Increasing the milling time over the range 5 to 35 h, the average size of the PZ particles decreases significantly, until at 25 h, the smallest particle size (estimated from SEM micrographs to be

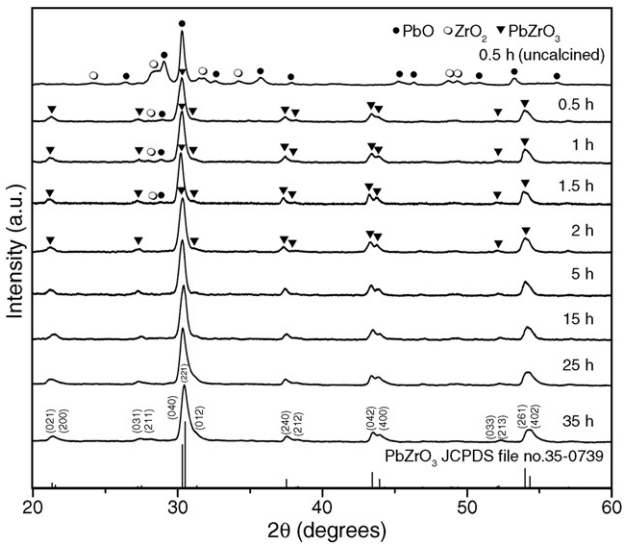

Fig. 2. XRD patterns of PZ powders milled at different times (calcined at 800 °C for 2 h with heating/cooling rates of 10 °C/min).

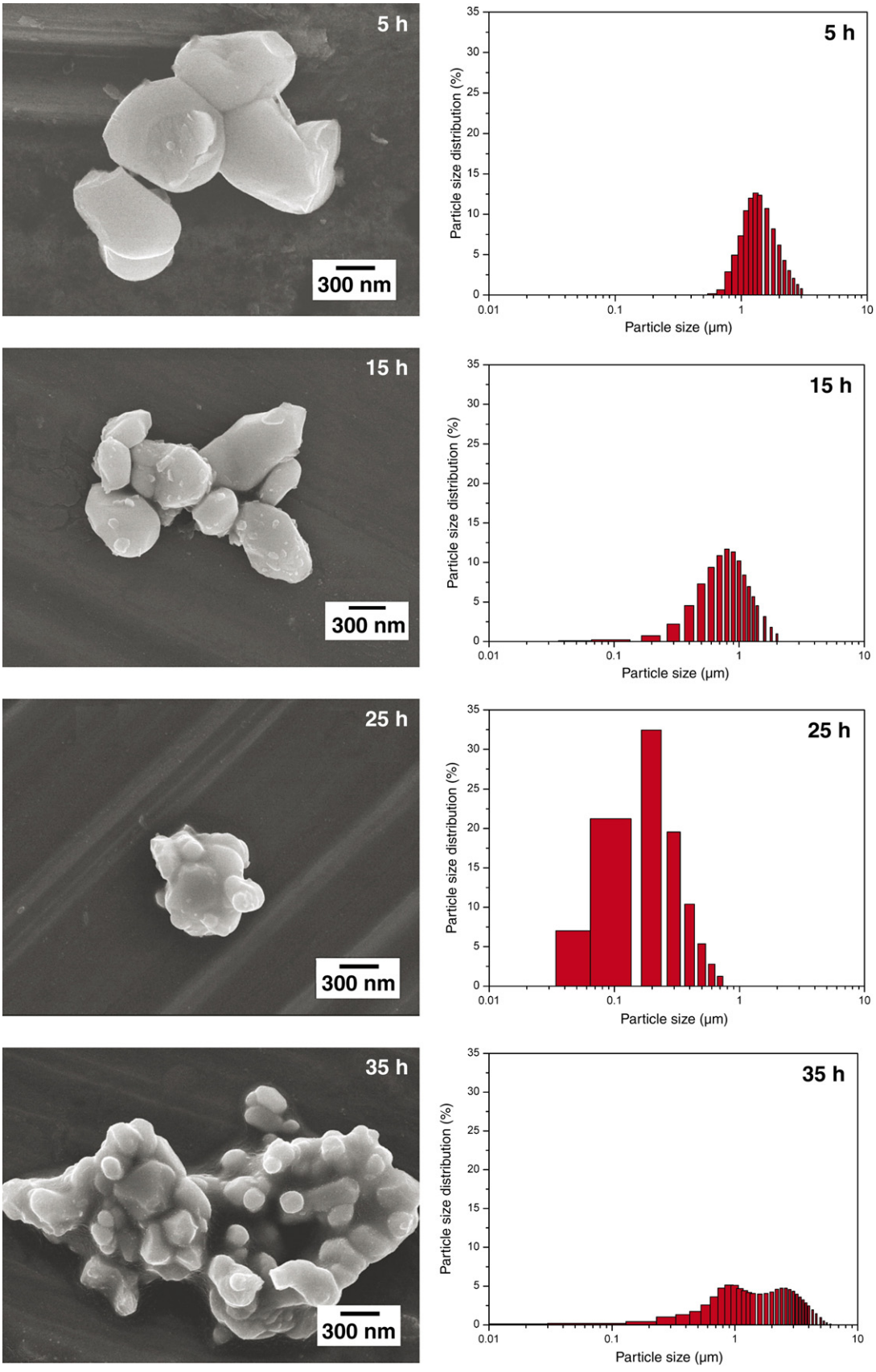

Fig. 3. SEM micrographs and particle size distribution of PZ powders milled at different times.

~50 nm) is obtained. However, it is also of interest to point out that a larger particle size was obtained for a milling time longer than 25 h. This may be attributed to the occurrence of hard agglomeration with strong inter-particle bonds within each aggregate resulting from dissipated heat energy of prolong milling [19]. Fig. 3 also illustrates that vibro-milling has slightly changed the shape of the particles which become more rounded at long milling times. At the same time, the particle size is reduced. Fracture is considered to be the major mechanism at long milling times.

As shown in Fig. 3, after milling times of 5 and 15 h, the powders have a similar particle size distribution. They exhibit a single peak covering the size ranging from 0.29 to 3.00 μm. With increasing milling times to 25 h, a uniform particle size distribution with a much lower degree of particle agglomeration (<1 μm) is found. However, upon further increase of milling time up to 35 h, a bimodal distribution curve with peak broadening between 0.24 and 6.20 μm is observed. First is a monomodal distribution corresponding to the primary size of the $PbZrO_3$ particles. The second group (peak) is believed to arise mainly from particle agglomeration. Table 1 compares the results obtained for PZ powders milled for different times via different techniques. Variations in these data may be attributed mainly to the formation of hard and large agglomerations found in the SEM results.

In this work, it is seen that the optimum milling time for the production of the smallest nanosized high-purity PZ powder was found to be at 25 h. The finding of this investigation indicates a strong relationship between the vibro-milling process and the yield of PZ nanopowders. However, in the case of the vibro-milling technique, other factors such as the milling speed, milling scale and type of milling media also need to be taken into account.

4. Conclusion

The results infer that the milling time influences not only the development of the solid-state reaction of lead zirconate phase but also the particle size and morphology. The resulting PZ powders have a range of particle size, depending on milling times. Production of a single-phase lead zirconate nanopowder can be successfully achieved by employing a combination of 25 h milling time and calcination condition of 800 °C for 2 h, with heating/cooling rates of 10 °C min^{-1}.

Acknowledgements

This work was supported by the National Nanotechnology Center (NANOTEC), the Royal Golden Jubilee Ph.D. Program, the Faculty of Science and the Graduate School of Chiang Mai University.

References

[1] B. Jaffe, W.R. Cook, H. Jaffe, Piezoelectric Ceramics, Academic Press, New York, 1971.
[2] F. Jona, G. Shirane, F. Mazzi, R. Pepinsky, Phys. Rev. 105 (1957) 849.
[3] T.R. Shrout, A. Halliyal, Am. Ceram. Soc. Bull. 66 (1987) 704.
[4] A.J. Moulson, J.M. Herbert, Electroceramics, 2nd ed.Wiley, Chichester, 2003.
[5] D.M. Ibrahim, H.W. Hennicke, Trans. J. Br. Ceram. Soc. 80 (1981) 18.
[6] E.E. Oren, E. Taspinar, A.C. Tas, J. Am. Ceram. Soc. 80 (1997) 2714.
[7] A. Rujiwatra, S. Tapala, S. Luachan, O. Khamman, S. Ananta, Mater. Lett. 60 (2006) 2893.
[8] E.R. Camargo, M. Popa, J. Frantti, M. Kakihana, Chem. Mater. 13 (2001) 3943.
[9] M.T. Lanagan, J.H. Kim, S. Jang, R.E. Newnham, J. Am. Ceram. Soc. 71 (1988) 311.
[10] R. Wongmaneerung, R. Yimnirun, S. Ananta, Mater. Lett. 60 (2006) 1447–1452.
[11] A. Udomporn, S. Ananta, Mater. Lett. 58 (2004) 1154.
[12] C. Puchmark, G. Rujijanagul, S. Jiansirisomboon, T. Tunkasiri, Ferroelectr. Lett. 31 (2004) 1.
[13] H. Klug, L. Alexander, X-Ray Diffraction Procedures for Polycrystalline and Amorphous Materials, 2nd ed.Wiley, New York, 1974.
[14] T. Aoyama, N. Kurata, K. Hiroto, O. Yamaguchi, J. Am. Ceram. Soc. 78 (1995) 3163.
[15] M.D. Johannes, D.J. Singh, Phys. Rev., B 71 (2005) 212101.
[16] Powder Diffraction File No. 35-0739. International Centre for Diffraction Data, Newtown Square, PA, 2000.
[17] C. Suryanarayana, Prog. Mater. Sci. 46 (2001) 1.
[18] A. Revesz, T. Ungar, A. Borbely, J. Lendvai, Nanostruct. Mater. 7 (1996) 779.
[19] P.C. Kang, Z.D. Yin, O. Celestine, Mater. Sci. Eng., A Struct. Mater.: Prop. Microstruct. Process. 395 (2005) 167.